

Article

# Authigenesis at the Urals Massive Sulfide Deposits: Insight from Pyrite Nodules Hosted in Ore Diagenites

Nataliya P. Safina \*, Irina Yu. Melekestseva, Nuriya R. Ayupova, Valeriy V. Maslennikov, Svetlana P. Maslennikova, Dmitry A. Artemyev and Ivan A. Blinov

South Urals Federal Research Center of Mineralogy and Geoecology UB RAS, Institute of Mineralogy, Chelyabinsk district, 456317 Miass, Russia; melekestseva-irina@yandex.ru (I.Y.M.); ayupova@mineralogy.ru (N.R.A.); maslennikov@mineralogy.ru (V.V.M.); svmas@mineralogy.ru (S.P.M.); artemyev@mineralogy.ru (D.A.A.); ivan\_a\_blinov@mail.ru (I.A.B.)

\* Correspondence: natali.safina2015@yandex.ru; Tel.: +7-950-726-92-75

Received: 26 December 2019; Accepted: 18 February 2020; Published: 20 February 2020



**Abstract:** The pyrite nodules from ore diagenites of the Urals massive sulfide deposits associated with various background sedimentary rocks are studied using optical and electron microscopy and LA-ICP-MS analysis. The nodules are found in sulfide–black shale, sulfide–carbonate–hyaloclastite, and sulfide–serpentinite diagenites of the Saf’yanovskoe, Talgan, and Dergamysh deposits, respectively. The nodules consist of the core made up of early diagenetic fine-crystalline (grained) pyrite and the rim ( $\pm$ intermediate zone) composed of late diagenetic coarse-crystalline pyrite. The nodules are replaced by authigenic sphalerite, chalcopyrite, galena, and fahlores (Saf’yanovskoe), sphalerite, chalcopyrite and galena (Talgan), and pyrrhotite and chalcopyrite (Dergamysh). They exhibit specific accessory mineral assemblages with dominant galena and fahlores, various tellurides and Co–Ni sulfoarsenides in sulfide–black shale, sulfide–hyaloclastite–carbonate, and sulfide–serpentinite diagenites, respectively. The core of nodules is enriched in trace elements in contrast to the rim. The nodules from sulfide–black shale diagenites are enriched in most trace elements due to their effective sorption by associated organic-rich sediments. The nodules from sulfide–carbonate–hyaloclastite diagenites are rich in elements sourced from seawater, hyaloclastites and copper–zinc ore clasts. The nodules from sulfide–serpentinite diagenites are rich in Co and Ni, which are typical trace elements of ultramafic rocks and primary ores from the deposit.

**Keywords:** pyrite nodules; ore diagenites; massive sulfide deposits; LA-ICP-MS analysis; diagenesis; anadiagenesis; Urals

## 1. Introduction

Diagenetic pyrite nodules are one of the types of sedimentary pyrite abundant in sedimentary sequences of various ages, in particular, in those enriched in organic matter [1–4]. They also occur in black shale sequences of gold deposits, where they are associated with arsenopyrite, native gold, and Au tellurides [1–3]. According to LA-ICP-MS analysis, the pyrite nodules, as a rule, are enriched in most trace elements (e.g., Au, As, Ni, Mn, Cu, Pb, Zn, Ag, Mo, Te, V, and Se) in comparison with hydrothermal and metamorphic pyrite varieties.

The formation mechanism of sedimentary (including nodular) pyrite is still a matter of debate [5–7]. Recent studies of syngenetic and diagenetic pyrite from black shales have showed that hydrothermal pyrite is a proxy of chemistry of ore-forming fluids, whereas sedimentary pyrite is an indicator of variable chemistry of seawater [8]. It is suggested that these pyrite types trapped trace elements from seawater (As, Hg, Ni, Mn, Pb, Co, Cu, Zn, Sb, Mo, Se, Ag, Tl, Bi, Te, and Au) and detrital matrix (Al, Ti,

Cr, V, P, Zr, Sn, Ba, W, Th, U) [2,9–11]. Although numerous morphological varieties of sedimentary pyrite exist, it exhibits only minor trace element variations [12].

Much less is known on pyrite nodules from massive sulfide deposits, where the nodules most often occur in associated sedimentary rocks (jaspers, black shales, cherts, etc.) and ore diagenites—banded sulfides with alternating monomineral layers of pyrite, pyrrhotite, carbonate, quartz, chlorite, and magnetite, which are recognized as seafloor altered clastic sulfide layers intercalated with pyrite cherts, chlorite shales and ferruginous halmyrolites [13]. In spite of the possible predicting role of trace element composition of pyrite nodules in searching for massive sulfide deposits, they are still poorly studied.

Few detailed studies of pyrite nodules from massive sulfide deposits are known to date. Significant variations in trace element composition within a pyrite nodule and its geochemical zoning were revealed for the Bracemac-McLeod massive sulfide deposits (Canada) [14]. The hanging wall sulfide–hyaloclastite sedimentary rocks (gossanites) of the Lahanos massive sulfide deposit (Pontides, Turkey) contain marcasite–pyrite nodules, the geochemical zoning of which reflects the composition of host rocks, ores, and primary background sediments [15]. The pyrite nodules from basaltic hyaloclastites of the Yubileynoe massive sulfide deposit (South Urals, Russia) also exhibit geochemical zoning [16]. Recently, the pyrite nodules have also been recognized in sulfide breccias from the Semenov-3 hydrothermal field of the Mid-Atlantic Ridge [17]. All cases show enrichment and depletion of central and marginal parts of the nodules in trace elements, respectively.

In this paper, we compare the morphology and mineralogical and geochemical features of pyrite nodules from pyrite- and pyrrhotite-rich diagenites of weakly metamorphosed massive sulfide deposits of the Urals, which are associated with different background sedimentary rocks: Saf'yanovskoe (black shales), Talgan (hyaloclastites, carbonates), and Dergamysh (clastic serpentinites). We will illustrate similar and distinct features of authigenic sulfide formation at massive sulfide deposits depending on the composition of associated background sediments.

## 2. Geological Outline

### 2.1. Regional Geology

The Urals is one of the world's largest orogenic belts, which extends for 2500 km from the Mugodzhary Mountains in the south to the Polar Urals in the north (Figure 1). It is traditionally subdivided into several structural zones, which represent different tectonic settings, including fragments of island arcs (Tagil Zone in the north and West and East Magnitogorsk zones in the south), inter-arc (Sibai Zone) and back-arc (Dombarovka, West Mugodzhary, Rezh) basins and a possible marginal sea (Sakmara Allochtone) (Figure 1) [18–20]. In the west, these Paleozoic ocean floor and island arc complexes are divided by the Main Uralian Fault Zone (MUFZ) from the Pre-Uralian, West Uralian, and Central Uralian zones, which represent the former margin of Baltica [21,22]. The MUFZ is considered to be one of the main suture zones of the Urals, marking the collision zone between the units belonging to the East European Continent in the west and the outboard terranes (arc) to the east.

All Paleozoic ocean floor and island arc complexes, as well as the MUFZ structure, host various massive sulfide deposits [18,23]. Generally, the most Urals massive sulfide deposits can be divided by host rock composition on mafic-ultramafic (Atlantic), mafic (Cyprus), bimodal-mafic (Uralian), and jaspers-associated (Baymak) and black shale-associated (Rudny Altai) bimodal-felsic types [20,24,25]. The deposits reviewed here belong to the Rudny Altai (Saf'yanovskoe), Uralian (Talgan), and Atlantic (Dergamysh) types. These three deposits are remarkable for the low degree of metamorphism (lower greenschist facies) of ores, which allows preservation of delicate hydrothermal structures [24–31].

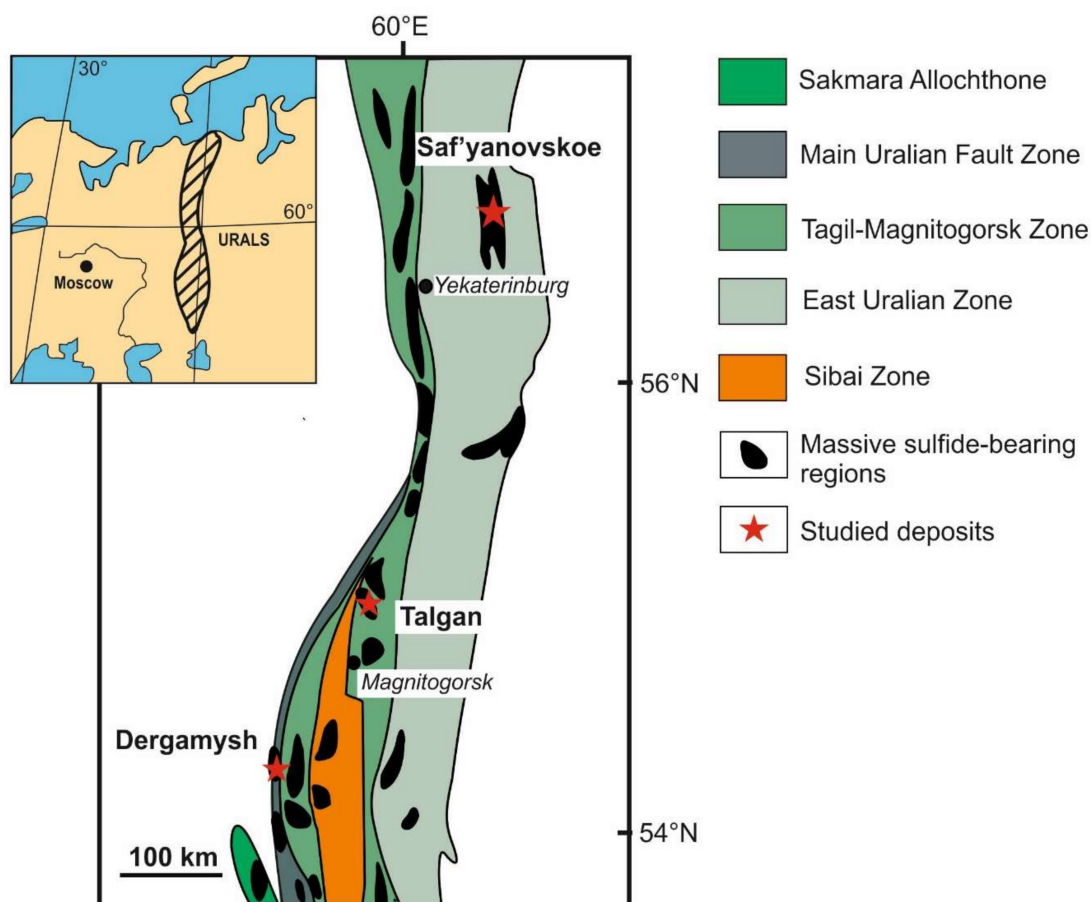


**Figure 1.** Geotectonic structure of the Urals and position of massive sulfide regions and studied deposits simplified after [26,32,33].

## 2.2. Saf'yanovskoe Deposit

The Saf'yanovskoe massive sulfide deposit is situated in the Sverdlovsk district, 9 km northeast of the town of Rezh in the Central Urals, and is confined to the East Uralian megazone (Figure 1). The deposit is thought to have formed in a Devonian back-arc basin [34]. The area of the deposit consists of a stack of three tectonic sheets (bottom to top): (i) up to a ~500 m-thick sheet composed of Late Devonian basalts and basaltic andesites, (ii) up to a ~500 m-thick ore-hosting sheet composed of Middle Devonian dacites and rhyolites, interlayered with volcanosedimentary rocks and black shales, and (iii) up to a ~300 m-thick sheet composed of Middle Devonian serpentinites, gabbro, limestones, and basalts, interlayered with Upper Devonian–Lower Carboniferous cherts (Figure 2a) [34,35].

The deposit includes 10 ore lenses up to 40 m-thick, which occur in three stratigraphic horizons at depths of 190 to 400 m (Figure 2a). In the central part of the deposit, the sulfide bodies are separated by sedimentary layers up to 10 m thick. At their margins, the sulfide bodies alternate with black shales up to 5 m thick (not shown in Figure 2a due to small sizes of their bodies). The main ore body is up to 400 m thick and is split on its flanks into several segments by subvolcanic rhyolite bodies [34,35]. Due to the low degree of metamorphism [35], the ores from the deposit contain fine-grained colloform varieties, smoker chimneys, and fossilized hydrothermal fauna [24,26,36].

The major vertical conical sulfide body, the core of which is composed of massive Cu–Zn ores with quartz–sphalerite–chalcopyrite black smoker chimneys, has been interpreted as a remnant sulfide mound [26]. The sulfide ores include massive Cu–Zn, Cu, and Fe types with dominant massive, banded, and breccia-like structures and stockwork Cu type consisting of a chalcopyrite–pyrite network in altered volcanic rocks. The thin ore layers are intercalated with black shales at the flanks of the deposit and form bedded bodies up to 20 cm thick.

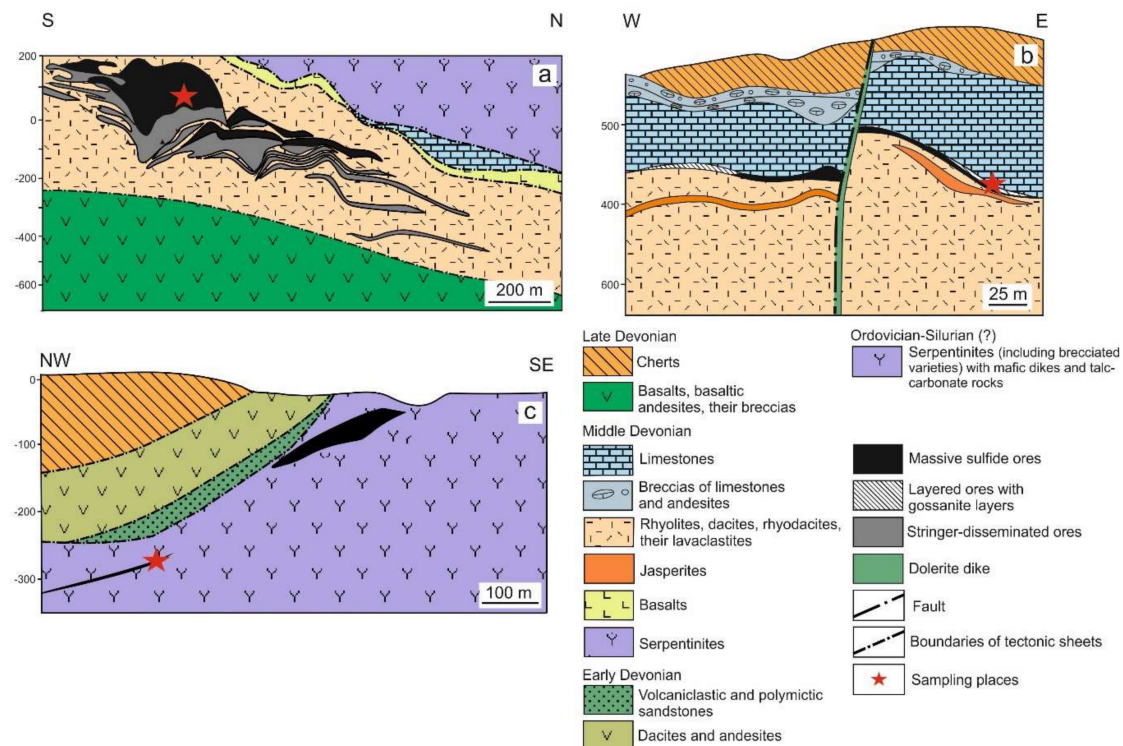


**Figure 2.** Geological cross-sections of the Saf'yanovskoe (a), Talgan (b), and Dergamysh (c) massive sulfide deposits (simplified from [27,28,37]).

### 2.3. Talgan Deposit

The Talgan massive sulfide deposit is situated in the Uzelga massive sulfide region in the South Urals within the West Magnitogorsk zone, which is interpreted as a Devonian island arc [20] (Figure 1). The geological section of the deposit consists of (bottom to top) a Middle Devonian rhyolite–dacite sequence 170–1000 m thick, a sequence 150–350 m thick composed of the Middle Devonian limestones and Upper Devonian volcanomictic andesite–basalt sandstones and cherts, and ore bodies at the contact of these two sequences (Figure 2b). The deposit hosts about 10 ore lenses 1–30 m thick, which occur at depths of 100–270 m. It is considered that these lenses were part of a single lenticular-bedded ore body divided by faults, rhyodacite intrusions, and dolerite dikes [38].

The Talgan ore bodies are interpreted as ore clastic lens with relics of a sulfide mound underlain by sericite–quartz metasomatites [39]. The relict sulfide mound is overlain by small-clastic ores and layered gossanites (ferruginous products of seafloor oxidation of massive sulfide ores) [24,26,30,39]. The slopes of the mound contain sulfide breccias with fragments of chalcopyrite–pyrite–sphalerite smoker chimneys, hydrothermal crusts, and fossilized tube worms. The fine-layered ores (including ore diagenites) are abundant at flanks of the deposit, where they form several horizons 2.5–2.8 m thick in total divided by chloritized hyaloclastites and gossanites.

The sulfide ores include (i) massive and brecciated pyrite and sphalerite–chalcopyrite–pyrite ores in the central part of the deposit, (ii) clastic barite–bornite–chalcopyrite–sphalerite ores at flanks of the deposit, and (iii) stockwork chalcopyrite–pyrite ores in altered volcanic rocks [26].

### 2.4. Dergamysh Deposit

The Dergamysh massive sulfide deposit is located in the MUFZ structure, 18 km northwest from the town of Buribay in the South Urals (Figure 1). It occurs within the western limb of an approximately N–S trending synform with gently-dipping western and steeply-dipping eastern limbs [27,40]. Several tectonic sheets, 50–500 m thick are distinguished at the deposit including (bottom to top) (Figure 2c) a sheet 300–500 m thick made of brecciated serpentinite with a layer of serpentinite sandstones

and conglomerates at its base, bodies of pegmatitic gabbros, fine-grained mafic dikes, blocks of talc-carbonate rocks, and a massive sulfide body with a thin cap of pillow hyaloclastite breccia at the top; a sheet > 70 m thick of Devonian volcanoclastic sediments, with interlayers of carbonaceous siltstones, sandstones, and platy serpentinite bodies; a sheet 100–150 m thick of Devonian andesites and dacites with transitional tholeiitic to calc-alkaline affinities; and the uppermost sheet > 300 m thick of Frasnian cherts.

The Dergamysh deposit consists of one large ore body and its two small satellites [27,40]. The main ore body dipping to the north is 150–200 m wide and up to 40 m thick (Figure 2c). The main ore body with chalcopyrite–marcasite, chalcopyrite–pyrite, and pyrite–marcasite ores is made up of three (in the south-east) or two (in the north-west) stacked lenses interfingering with thin layers of brecciated serpentinites and chloritized mafic rocks. The two satellite ore bodies (satellite-1 and -2) were encountered within the same tectonic sheet 200 m and, respectively, 500 m north-west of the main ore body. Satellite-1 ore body is represented by a 20-cm thick sulfide layer in massive serpentinites. Satellite-2 ore body includes both massive and stockwork ores in serpentinites. Host rocks are altered with formation of talc, quartz, carbonates, and chlorite. The main ore body was interpreted as a strongly eroded sulfide mound with fragments of numerous chalcopyrite–pyrite and calcite–pyrite-rich chimneys, diffusers-like structures, colloform sulfides, and fossilized tube worms [24,25]. The upper part of the main ore body is composed of coarse-clastic pyrite breccias with fragments of chalcopyrite–pyrite smoker chimneys, which are crowned by fine (1–10, rare, up to 20 cm thick) interlayers of sulfide gravelites and sandstones intercalated with siltstones.

### 3. Materials and Methods

Samples with pyrite nodules were collected in the open pit of the Saf'yanovskoe deposit, the mine of the Talgan deposit, and borehole 200 of the Dergamysh deposit. All samples were studied macroscopically and then using reflected light microscopy at the South Urals Federal Research Center of Mineralogy and Geoecology UB RAS, Institute of Mineralogy (IMin) (Miass, Russia). The microinclusions of minerals in pyrite nodules were also identified on a Vega 3sbu Tescan SEM equipped with a Link ED system (IMin).

Quantitative LA-ICP-MS analysis of trace elements ( $^{51}\text{V}$ ,  $^{52}\text{Cr}$ ,  $^{55}\text{Mn}$ ,  $^{59}\text{Co}$ ,  $^{60}\text{Ni}$ ,  $^{65}\text{Cu}$ ,  $^{66}\text{Zn}$ ,  $^{75}\text{As}$ ,  $^{77}\text{Se}$ ,  $^{95}\text{Mo}$ ,  $^{107}\text{Ag}$ ,  $^{111}\text{Cd}$ ,  $^{118}\text{Sn}$ ,  $^{121}\text{Sb}$ ,  $^{125}\text{Te}$ ,  $^{182}\text{W}$ ,  $^{197}\text{Au}$ ,  $^{205}\text{Tl}$ ,  $^{208}\text{Pb}$ ,  $^{209}\text{Bi}$ ,  $^{232}\text{Th}$ ,  $^{238}\text{U}$ ) was carried out on a New Wave 213-nm solid-state laser microprobe coupled to an Agilent 7700 quadrupole ICP-MS housed at the CODES LA-ICP-MS analytical facility (University of Tasmania, Hobart, Australia) for the Talgan deposit and a New Wave Research UP 213-nm solid-state laser microprobe coupled to an Agilent 7700X ICP-MS (IMin) for the Saf'yanovskoe and Dergamysh deposits.

The CODES LA-ICP-MS analyses were performed by ablating spots ranging in size from 15 to 20  $\mu\text{m}$ . The laser repetition rate was 5 Hz and laser beam energy at the sample was maintained between 4 and 5  $\text{J}/\text{cm}^2$ . The analysis time for each spot was 100 s, comprising a 30-s measurement of background (laser off) and a 70-s measurement with laser on. Acquisition time for all masses was set to 0.02 s. Data reduction was undertaken according to standard methods [41]. Iron was used as the internal standard for quantification of pyrite. Concentrations of the internal standard were calculated assuming stoichiometry. In cases when a significant degree of fine-grained mineral intergrowth occurred within the ablated volume, values for the internal standard concentration were adjusted such that the total of major elements (Fe, Cu, Zn, and S, the latter calculated assuming stoichiometry) is 100%. Detection limits were calculated as three times the standard error for the count rates of the instrument background signal (laser-off). An in-house Li-borate fused glass of a pyrite/sphalerite mixture [42] was used as the primary calibration standard. To account for the instrument drift, the standard was analyzed twice every one and a half hours, using a 100  $\mu\text{m}$  beam and a repetition rate of 10 Hz, thus closely maintaining the aspect ratio between ablation craters on the samples and on the standard.

The IMin LA-ICP-MS analyses were performed by ablating spots ranging in size from 15 to 20  $\mu\text{m}$ . Laser repetition rate was 10 Hz and laser beam energy at the sample was maintained between 3 and

4 J/cm<sup>2</sup>. The analysis time for each spot was 75–80 s, comprising a 20–30 s measurement of background (laser off) and a 45–60 s measurement with laser on. The mass-spectrometer was calibrated using multi-elemental solutions. The trace element contents were calculated in an Iolite program using international glass (BCR-2G, GSD-1G) and sulfide (MASS-1) standards and <sup>57</sup>Fe as the internal standard for quantification of pyrite (46.5%). The LA-ICP-MS data were processed in Statistica program v.10 using correlation analysis.

LA-ICP-MS mapping was conducted using the same device at the IMin at a laser beam energy of 3.5–4.5 J/cm<sup>2</sup>, a laser repetition rate of 10 Hz, a carrier gas of He, and a flow rate of 0.65 L/min. The trace element maps were plotted using Iolite program and are based on signal intensity during consecutive ablation of the nodule area with a laser beam of 12 μm moving at a rate of 10 μm/s and a distance between ablation profiles of 12 μm. Both line and map analyses of pyrite were calibrated against MASS-1, a U.S. Geological Survey reference material, using values published in [43]. Iron was the internal standard. Previously, a relatively round pyrite nodule with clear zoning was studied for the Talgan deposit [44]. For this study, we chose a pyrite nodule, which is more morphologically similar to Saf'yanovskoe pyrite nodules with less clear zoning and a wider outer zone composed of coarse-crystalline pyrite.

The LA-ICP-MS analyses of pyrite and pyrrhotite were processed in Statistica v.10 program using correlation analysis in order to identify trace element associations (see Section 5.3), which were ordered from maximum to minimum coefficient of correlation according to the method of [45].

## 4. Results

### 4.1. Mode of Occurrence of Pyrite Nodules in Ore Diagenites

#### 4.1.1. Saf'yanovskoe Deposit

The sulfide nodules of the Saf'yanovskoe deposit were found in pyrite-rich sulfide–black shale diagenites at the southern flank of the deposit, which represent an intercalation of sulfide layers (1–3 cm thick) and black shale layers (up to 3.5 wt. % C<sub>org</sub> [46]) with a thickness from few millimeters to 1 cm (Figure 3a). These black shale layers host rare large flattened azoned sulfide nodules up to 0.5 cm in size, which are found along the bedding. Thinner black shale layers (few millimeters thick) contain numerous small elongated or round nodules up to 1–2 mm in diameter (Figure 3b,c), pyrite framboids up to 100 μm in diameter, and pyrite crystals up to 70 μm in size. In sulfide layers, all these morphological forms of pyrite are dominant in the top of the layers.

Small elongated pyrite nodules (up to 0.4 mm in size) from black shale layers show zoned structure including three zones (Figure 3b). The core (zone A) is composed of fine-crystalline pyrite aggregate (Py1saf) made up of euhedral and subhedral pyrite crystals (1–2 μm) and rare pyrite framboids (5–7 μm) in a nonsulfidic matrix with numerous inclusions of chlorite, hydromicas, sphalerite, and chalcopyrite (Figure 3b,c). This zone is gradually replaced by anhedral small-grained pyrite (Py2saf) (intermediate zone B) with numerous inclusions of galena, altaite, fahlore, covellite, and rare chalcopyrite and sphalerite (Figure 3d,e). The zone B is often undistinguishable under an optical microscope, but it is clearly seen under an electron microscope due to numerous inclusions of authigenic minerals (Figure 3e). Its presence is also supported by geochemical mapping (see below). A rim (zone C) up to 50–60 μm thick is made up of coarser-crystalline subhedral pyrite (Py3saf) with rare inclusions of quartz, rutile, galena, and arsenopyrite (Figure 3f). The matrix hosts pyrite framboids, pyrite and arsenopyrite crystals, anhedral chalcopyrite grains, pyrite–chalcopyrite intergrowths with inclusions of galena, and sphalerite clasts with fahlore and enargite inclusions (Figure 3c).

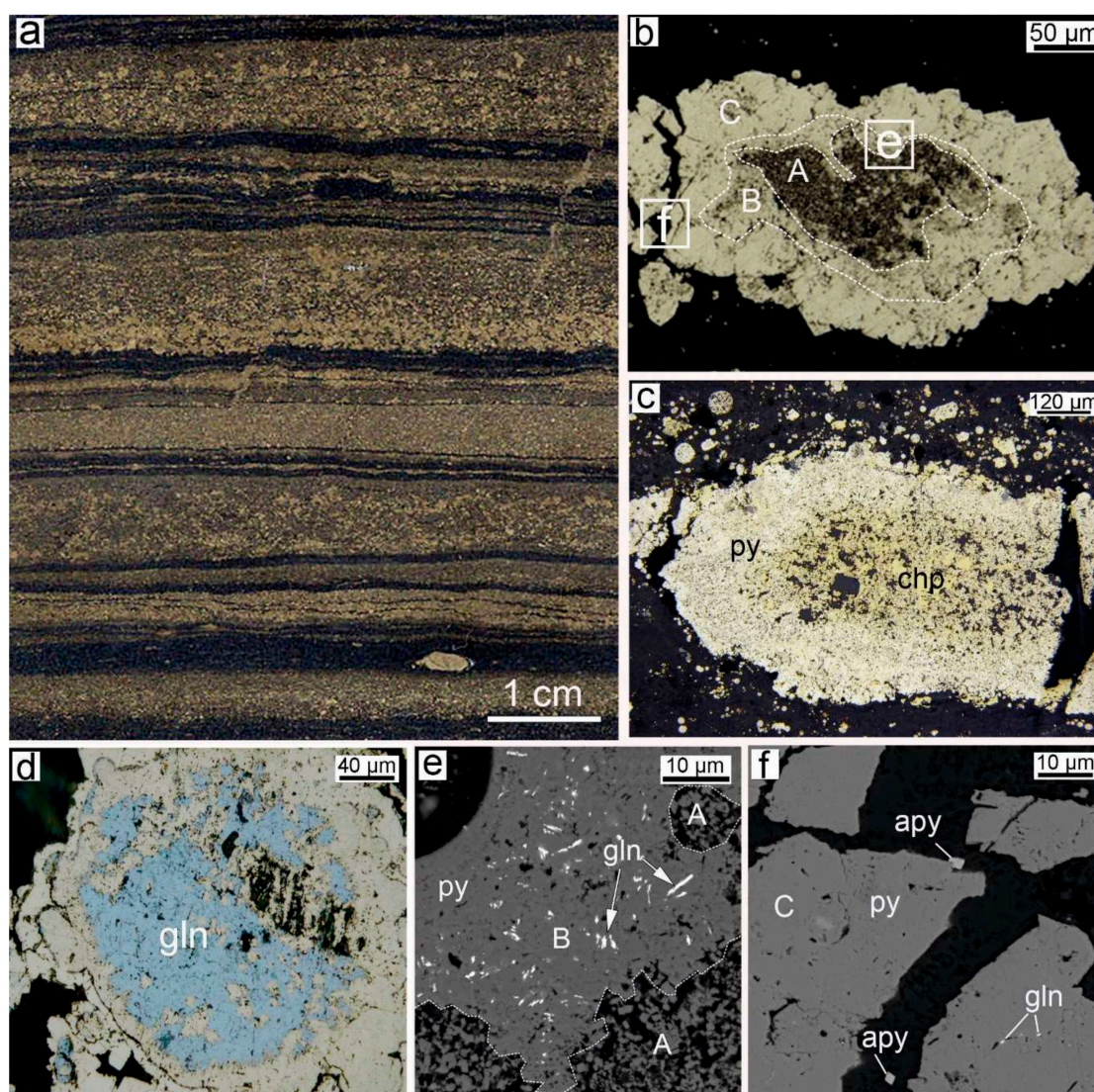


**Figure 3.** Pyrite nodules in sulfide–black shale diagenites of the Saf'yanovskoe deposit: (a) sulfide–black shale diagenite with intercalated sulfide and black shale layers, polished sample; (b) zoned pyrite nodule with the core (zone A), intermediate zone (zone B) and the rim (zone C); (c) replacement of fine-grained pyrite (py) from the core by chalcopyrite (chp); (d) replacement of the nodule by galena (gln); (e) numerous galena inclusions in zone B (detail of photo b); (f) fragment of zone C with galena and arsenopyrite (apy) inclusions (detail of photo b). Reflected light (b–d); SEM-photo (e,f).

#### 4.1.2. Talgan Deposit

Pyrite nodules of the Talgan deposit were found in thin-layered pyrite-rich sulfide–carbonate–hyaloclastite diagenites, which occur around an interpreted sulfide mound of the deposit [26,44]. At the distance from the sulfide mound, the thickness of diagenites decrease from 1–2 m to a few centimeters. To the east and the southeast of the sulfide mound, the diagenites form two horizons 0.5–2.8 m thick divided by brightly red layers of gossanites and chloritized hyaloclastites. Here, the diagenites represent the rhythmical intercalation of sulfide layers (up to a few centimeters thick) and pelitic carbonate–hyaloclastite layers (up to 0.5 mm thick) (Figure 4a).

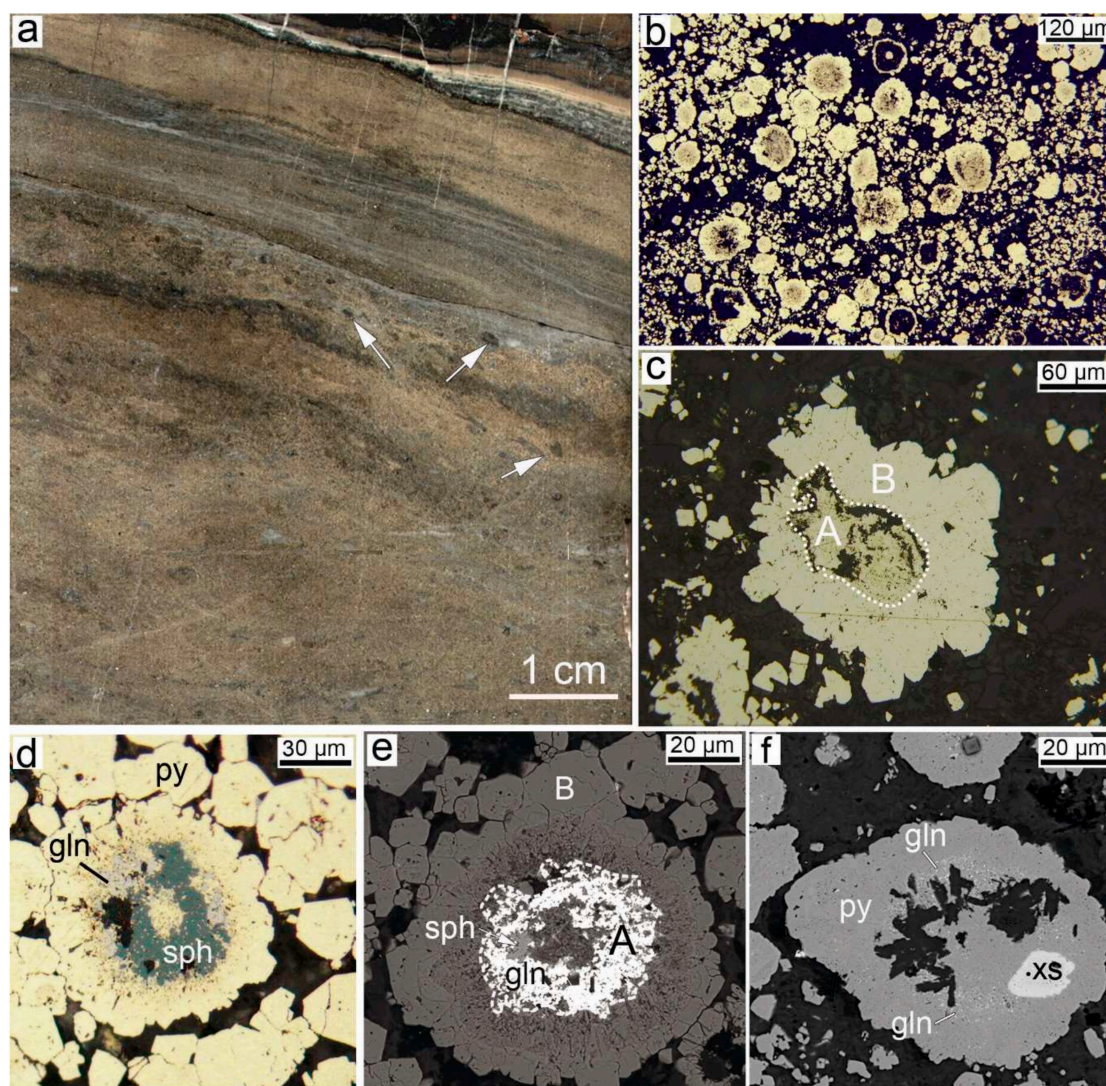


**Figure 4.** Pyrite nodules in sulfide–carbonate–hyaloclastite diagenites of the Talgan deposit: (a) sulfide–carbonate–hyaloclastite diagenite with thick sulfide layers, thin carbonate–hyaloclastite interlayers (gray and black), and chloritized hyaloclasts (indicated by arrows), polished sample; (b) pyrite nodules and crystals in sulfide layers; (c) zoned pyrite nodule in carbonate–hyaloclastite matrix; (d,e) replacement of fine-grained pyrite (py) from the core by sphalerite (sph) and galena (gln); (f) galena and xenotime (xs) inclusions in pyrite nodules. Reflected light (b–d); SEM-photo (e,f).

The round and angular pyrite nodules 30–200  $\mu\text{m}$  in diameter with rare syneresis cracks are unevenly distributed amid subhedral and euhedral pyrite crystals and, locally, pseudomorphic pyrite after pyrrhotite crystals (5–50  $\mu\text{m}$ ) in a carbonate–hyaloclastite matrix of diagenites composed of quartz, calcite, chlorite, and illite (Figure 4b) with inclusions of anhedral aggregates of sphalerite, chalcopryrite, barite, and rare tennantite and scheelite. The nodules exhibit a zoned structure with two zones. The core (zone A) is typically composed of fine-grained pyrite (Py1tg) with numerous inclusions of chlorite, illite, calcite, rutile, galena, sphalerite, and chalcopryrite (Figure 4). The zone B up to 20–30  $\mu\text{m}$  thick is made up of fine-grained to more compact small-grained homogeneous pyrite or coarser parallel-columnar subhedral pyrite (Py2tg) with inclusions of galena, chalcopryrite, galena, and xenotime (Figure 4). In some layers, pyrite of zones A and B is replaced by nonsulfidic minerals or crystalline pyrite. The pyrite nodules and carbonate–hyaloclastite matrix are also host to inclusions of REE minerals (bastnaesite, synchisite, parisite, xenotime) (Figure 4f) [47].

#### 4.1.3. Dergamysh Deposit

Pyrite nodules of the Dergamysh deposit were recognized in the satellite-1 ore body at the northwest part of the deposit, which is represented by a 20-cm thick pyrite–chalcopyrite–pyrrhotite layer (pyrrhotite-rich diagenite [13]) mixed with serpentinite fragments up to 5 cm across [27,40]. Macroscopically, this layer exhibits a clastic structure with angular fragments of pyrite and pyrrhotite 1–4 mm in size and interstitial chalcopyrite aggregates in a rock-forming and small-grained sulfide matrix (Figure 5a), however, pyrrhotite, chalcopyrite, and cubanite have pseudomorphic nature and probably replaced former pyrite clasts (Figure 5b–d) [13]. The sulfide aggregates are also replaced by quartz and magnetite. The primary clastic origin of satellite-1 ore body is supported by numerous chromite clasts (Figure 5c). This layer contains accessory minerals such as pentlandite inclusions in pyrrhotite aggregates, mackinawite lamellae in pseudomorphic chalcopyrite, associated nickeline, gersdorffite, cobaltite, native gold, and pilsenite at the contacts of chalcopyrite and pyrrhotite, chalcopyrite, and nonsulfidic minerals [40].

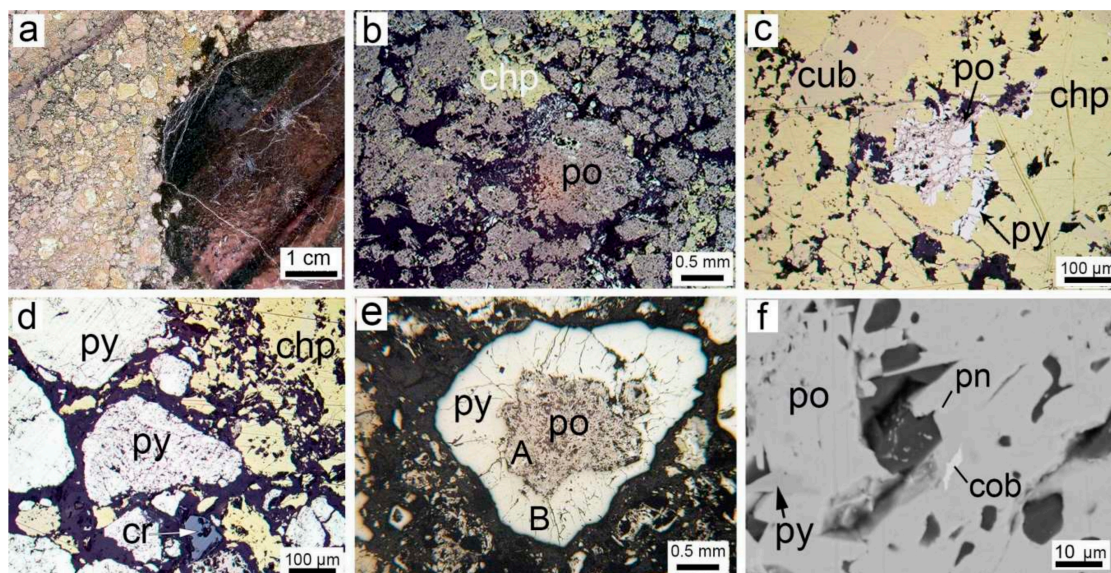


**Figure 5.** Pyrite nodules in sulfide–serpentinite diagenites of the Dergamysh deposit: (a) fragment of sulfide–serpentinite diagenite of the Dergamysh deposit, drill core sample; (b) pseudomorphic pyrrhotite (po) and chalcopyrite (chp) after former pyrite (small white areas inside pyrrhotite); (c) replacement of pyrite (py) by pyrrhotite and further by cubanite (cub)–chalcopyrite aggregates; (d) clastic textural pattern made up by angular pyrite and chromite (cr) sealed by interstitial chalcopyrite; former pyrite clast with cut textural pattern (from the bottom) is completely replaced by pyrrhotite and later crystalline pyrite; (e) zoned pyrrhotite–pyrite nodule with an open-latticework pyrrhotite aggregate in the core (zone A—former fine-crystalline or fine-grained pyrite) and a rim of coarse-crystalline pyrite (zone B); (f) cobaltite (cob), pentlandite (pn), and pyrite inclusions in pseudomorphic pyrrhotite. Reflected light (b–e), SEM image (f).

Numerous lenticular and smoothed angular nodules from few hundreds of micrometers to 3 mm in size are characterized by a porous core (zone A) composed of pseudomorphic open-latticework pyrrhotite aggregates (Podg), which is surrounded by a rim of crystalline pyrite (Pydg) (zone B) (Figure 5e). In many cases, the cores of the nodules are replaced nonsulfidic minerals. Fine pyrite, chalcopyrite, pentlandite, and cobaltite inclusions are observed in the core of the nodules (Figure 5f–h). Fragmented pyrite crystals of the rims are crossed by pyrrhotite veinlets a few micrometers thick. Pyrrhotite also replaces pyrite crystals along the growth zones.

#### 4.2. Trace Element Composition of Pyrite Nodules

Pyrite types (as well as pyrrhotite) from sulfide nodules of sulfide–black shale diagenites of the Saf'yanovskoe deposit, sulfide–carbonate–hyaloclastite diagenites of the Talgan deposit, and sulfide–serpentinite diagenites of the Dergamysh deposit (hereinafter, sulfide–black shale, sulfide–carbonate–hyaloclastite, and sulfide–serpentinite diagenites, respectively) exhibit specific geochemical features (Table 1, Figure 6, Supplementary Material). The description of trace element composition follows the position of trace elements in Table 1 and intimately correlated trace elements (e.g., Co and Ni; Zn and Cd; Ag and Au; Pb, Bi, and Te) are described together. The trace element contents in text are presented as median values if not specified.

*Ti.* The Ti contents of pyrite types of nodules vary from 0.1 to 246 ppm. In the nodules of sulfide–black shale and sulfide–carbonate–hyaloclastite diagenites, the high Ti contents are typical of the coarse-crystalline (Py3saf) and fine-grained (Py1tg) pyrite, respectively (Figure 6). Other pyrite types exhibit low Ti contents.

*V.* The V contents of nodular sulfides from all diagenite types are generally low (0.02–27 ppm). Their highest values are typical of fine-crystalline pyrite from sulfide–black shale (Py1saf) and sulfide–carbonate–hyaloclastite (Py1tg) diagenites (Figure 6). The V contents of crystalline pyrite of all nodules of sulfide–black shale and sulfide–carbonate–hyaloclastite diagenites and pyrrhotite from sulfide–serpentinite diagenites (Podg) are low.

*Cr.* All pyrite types and pyrrhotite of nodules are generally characterized by low Cr contents (max 14 ppm). Slightly higher Cr contents are detected in fine-crystalline and fine-grained pyrite relative to the lower Cr contents of coarse-crystalline pyrite (Figure 6). The most variable Cr contents are typical of pyrrhotite from sulfide–serpentinite diagenites.

*Mn.* The highest Mn contents are registered in fine-crystalline pyrite (Py1saf) from sulfide–black shale diagenites (541 ppm) in contrast to small-grained pyrite (Py2saf) and coarse-crystalline pyrite (Py3saf) (56.2 and 120 ppm, respectively) (Figure 6). The fine-grained pyrite (Py1tg) and coarse-crystalline pyrite (Py2tg) from sulfide–carbonate–hyaloclastite diagenites exhibit similar Mn contents (212 and 257 ppm, respectively). The lowest Mn contents are typical of pyrite and pyrrhotite nodule from sulfide–serpentinite diagenites.

*Co and Ni.* The fine-grained pyrite (Py1tg) from sulfide–carbonate–hyaloclastite diagenites and pyrrhotite (Podg) and coarse-crystalline pyrite (Pydg) from sulfide–serpentinite diagenites are characterized by the highest contents of Co (1106, 873, and 616 ppm, respectively) and Ni (404, 990, and 709 ppm, respectively) and the highest Co/Ni ratio of ~1 (Figure 6). The lowest Co (49.1 ppm) and high Ni (586 ppm) contents at a Co/Ni ratio of 0.01 are typical of fine-crystalline pyrite (Py1saf) from sulfide–black shale diagenites. The late pyrite types from both sulfide–black shale and sulfide–carbonate–hyaloclastite diagenites (Py2saf, Py3saf, and Py2tg) have the lowest Co and Ni contents (Figure 6).

*Cu.* The highest Cu contents (0.9 wt. %) are detected in coarse-crystalline pyrite (Py2tg) from sulfide–carbonate–hyaloclastite diagenites. The lower Cu contents (846 ppm) of fine-grained pyrite (Py1tg) from sulfide–carbonate–hyaloclastite diagenites are comparable with those from all pyrite types of sulfide–black shale diagenites (0.12 wt. % in Py1saf, 791 ppm Py2saf, and 561 ppm in Py3saf) (Figure 6). The lowest Cu contents (64 and 144 ppm) are typical of pyrrhotite (Podg) and coarse-crystalline pyrite (Pydg) from sulfide–serpentinite diagenites, respectively (Figure 6).

*Zn and Cd.* The distribution of these elements is similar in pyrite of nodules studied (Figure 6). The fine-crystalline and fine-grained pyrite of the nodules is characterized by wide variations in Zn and Cd contents (0.83 ppm to 8.3 wt. % and 0.01 to 622 ppm, respectively). Both Zn and Cd contents strongly decrease in a range from early to late pyrite (Figure 6). The lowest Zn and Cd contents are detected in pyrrhotite (Podg) and coarse-crystalline pyrite (Pydg) from sulfide–serpentinite diagenites.

**Table 1.** Trace element content (ppm) of pyrite and pyrrhotite of the nodules from Saf’yanovskoe, Talgan, and Dergamysh massive sulfide deposits.

Values	Ti <sup>49</sup>	V <sup>51</sup>	Cr <sup>53</sup>	Mn <sup>55</sup>	Co <sup>59</sup>	Ni <sup>60</sup>	Cu <sup>65</sup>	Zn <sup>66</sup>	As <sup>75</sup>	Se <sup>77</sup>	Mo <sup>95</sup>	Ag <sup>107</sup>	Cd <sup>111</sup>	Sn <sup>118</sup>	Sb <sup>121</sup>	Te <sup>125</sup>	Ba <sup>137</sup>	W <sup>182</sup>	Au <sup>197</sup>	Tl <sup>205</sup>	Pb <sup>208</sup>	Bi <sup>209</sup>	U <sup>238</sup>
Saf’yanovskoe deposit, fine-crystalline poikilitic pyrite (Py1saf) (n = 9)																							
min	0.1	3.1	2.8	210	33.0	473	628	130	0.25 *	172	58.1	149	1.5	0.2	61.5	0.4	11.7	0.01	10.2	11.6	0.1 *	19.9	0.03
max	17.5	21.8	13.4	932	58.7	747	2.1 *	3.6 *	0.36	360	230	335	236	18.9	101	5.6	68	0.02	46.4	28.0	0.76 *	35.5	0.26
av	4.8	11.2	7.32	552	46.8	599	0.5 *	0.8 *	0.32	228	120	220	50.4	6.79	80.0	2.81	43.2	0.01	32.5	18.6	0.3 *	26.6	0.10
σ	3.78	5.73	2.34	123	7.3	87.8	0.5 *	0.6 *	232	40.7	43.7	37.8	46.4	5.32	12.5	1.30	18.2	0.01	7.1	3.9	0.2 *	4.23	0.06
med	3.50	8.2	7.30	541	46.7	581	0.12 *	0.5 *	0.3 *	218	97.0	206	29.0	4.80	74.6	2.40	49.2	0.01	36.2	17.7	0.2	24.3	0.08
Saf’yanovskoe deposit, anhedral small-grained pyrite (Py2saf) (n = 5)																							
min	9.0	1.92	2.1	46.2	1.52	66.4	624	12	0.3 *	17.9	38.7	162	0.04	0.05	31.9	0.08	5.1	0.01	2.50	7.53	805	5.1	0.05
max	97	10.8	6.5	318	16.7	233	1530	198	0.6 *	159	156	227	2.1	1.58	77.2	4.8	44	0.27	7.4	20.2	0.7 *	23.4	0.78
av	34.3	5.69	3.60	107	8.79	149	939	98.5	0.5 *	66.2	77.1	184	0.79	0.80	51.4	1.83	19.8	0.10	4.10	11.6	0.3 *	11.4	0.30
σ	28.6	2.85	1.24	84.4	5.24	63.1	291	69.0	544	48.5	38.1	18.2	0.59	0.51	15.5	1.65	11.2	0.10	1.61	4.1	0.2 *	6.33	0.23
med	11.4	6.56	3.00	56.2	8.00	158	791	121	0.50 *	30.1	49.1	176	0.77	0.78	52.9	1.17	21.3	0.02	3.25	8.8	0.3 *	8.14	0.15
Saf’yanovskoe deposit, subhedral coarser-crystalline pyrite (Py3saf) (n = 20)																							
min	1.1	0.21	0.14	41.6	0.21	14.2	384	9.8	0.4 *	11.4	13.4	129	0.01	0.18	8.74	0.02	0.54	0.01	2.33	4.63	136	0.73	0.01
max	230	3.99	3.14	187	10.7	180	1500	500	0.9 *	61.3	122.4	247	2.6	0.67	57.8	2.5	20.1	0.4	5.0	14.6	0.5 *	12.8	1.54
av	30.5	1.79	1.55	107	4.4	73.6	662	58.0	0.7 *	25.8	40.9	165	0.28	0.41	26.21	0.68	7.25	0.05	3.3	7.58	0.1 *	5.4	0.26
σ	25.0	0.79	0.64	43.3	2.74	36.8	223	66.7	0.2 *	10.9	26.9	23.6	0.37	0.15	11.1	0.52	3.28	0.05	0.6	2.0	0.1 *	2.6	0.24
med	18.3	1.71	1.38	120	3.80	60.3	561	13.5	0.8 *	21.4	22.05	159	0.01	0.36	22.4	0.42	6.10	0.01	3.12	6.89	756	4.36	0.13
Saf’yanovskoe deposit, all sulfides (n = 34)																							
min	0.1	0.21	0.14	41.6	0.21	14.2	384	9.8	0.25 *	11.4	13.4	129	0.01	0.05	8.74	0.02	0.54	0.01	2.33	4.63	136	0.73	0.01
max	230	21.8	13.4	932	58.7	747	2.1 *	3.6 *	0.9 *	360	230	335	236	18.9	101	5.6	68	0.4	46.4	28.0	0.8 *	35.5	1.54
av	24.3	4.85	3.38	225	16.3	224	0.2 *	0.2 *	0.6 *	85.4	67.1	182	13.6	2.16	44.1	1.41	18.6	0.05	11.2	11.1	0.2 *	11.9	0.22
	Ti <sup>49</sup>	V <sup>51</sup>	Cr <sup>53</sup>	Mn <sup>55</sup>	Co <sup>59</sup>	Ni <sup>60</sup>	Cu <sup>65</sup>	Zn <sup>66</sup>	As <sup>75</sup>	Se <sup>77</sup>	Mo <sup>95</sup>	Ag <sup>107</sup>	Cd <sup>111</sup>	Sn <sup>118</sup>	Sb <sup>121</sup>	Te <sup>125</sup>	Ba <sup>137</sup>	W <sup>182</sup>	Au <sup>197</sup>	Tl <sup>205</sup>	Pb <sup>208</sup>	Bi <sup>209</sup>	U <sup>238</sup>
σ	21.9	4.05	2.36	180	16.2	199	0.2 *	0.3 *	0.2 *	80.6	42.0	31.8	21.2	2.70	24.5	1.24	15.4	0.05	11.4	4.94	0.15 *	8.71	0.19
med	12.6	2.44	2.23	136	6.69	94.4	770	31.2	0.5 *	29.7	51.8	175	0.24	0.51	33.6	0.63	10	0.01	3.58	8.43	0.15 *	7.0	0.11

Table 1. Cont.

Values	Ti <sup>49</sup>	V <sup>51</sup>	Cr <sup>53</sup>	Mn <sup>55</sup>	Co <sup>59</sup>	Ni <sup>60</sup>	Cu <sup>65</sup>	Zn <sup>66</sup>	As <sup>75</sup>	Se <sup>77</sup>	Mo <sup>95</sup>	Ag <sup>107</sup>	Cd <sup>111</sup>	Sn <sup>118</sup>	Sb <sup>121</sup>	Te <sup>125</sup>	Ba <sup>137</sup>	W <sup>182</sup>	Au <sup>197</sup>	Tl <sup>205</sup>	Pb <sup>208</sup>	Bi <sup>209</sup>	U <sup>238</sup>
Talga deposit, fine-grained poikilitic pyrite (Py1tg) (n = 7)																							
min	4.9	5.0	0.02	94	260	197	571	145	849	0.1	0.2	143	4.0	0.1	234	16	1.00	6.0	0.02	0.8	1046	1.6	0.02
max	246	27.0	2.4	981	1802	738	1162	8.3 *	0.17 *	1.0	2.5	660	622	0.8	5394	103	33.0	42	0.17	13.1	10.0 *	32.1	0.53
av	67	15.9	1.42	292	1026	456	847	1.31 *	0.13 *	0.50	1.0	390	102	0.4	1603	55	10.7	25	0.09	6.6	2.4	9.8	0.23
σ	62	6.12	0.49	197	553	175	156	2.00 *	286	0.29	0.71	195	149	0.2	1634	27	8.2	10.5	0.05	4.25	2.7 *	7.4	0.16
med	40	15.0	1.6	212	1106	404	846	251	1468	0.30	0.7	504	4.9	0.4	551	58	9.0	25	0.12	7.4	0.6 *	7.1	0.18
Talga deposit, subhedral coarse-crystalline pyrite (Py2tg) (n = 7)																							
min	1.5	0.03	0.04	93	0.03	3	0.2 *	3	18	0.1	0.01	10	0.3	0.01	9	0.05	0.04	4.9	0.01	0.1	41	0.1	0.01
max	2.5	0.7	0.8	2422	1.0	19	1.4 *	19	378	0.6	0.10	90	11	0.1	136	3.0	4.40	58	0.01	6.0	7036	2.5	0.02
av	1.99	0.2	0.31	734	0.38	6.86	0.8 *	9	135	0.31	0.07	38	2.76	0.04	54.6	0.64	1.89	25	0.01	1.63	1782	0.66	0.01
σ	0.33	0.14	0.17	771	0.36	3.55	0.3 *	5.4	84.2	0.13	0.04	25	2.36	0.03	34.2	0.69	1.21	11.4	0.002	1.47	1747	0.77	0.004
med	2.1	0.1	0.3	257	0.1	5	0.9 *	7	112	0.3	0.1	23	1.7	0.03	58	0.20	2.00	24	0.01	0.9	769	0.1	0.01
	Ti <sup>49</sup>	V <sup>51</sup>	Cr <sup>53</sup>	Mn <sup>55</sup>	Co <sup>59</sup>	Ni <sup>60</sup>	Cu <sup>65</sup>	Zn <sup>66</sup>	As <sup>75</sup>	Se <sup>77</sup>	Mo <sup>95</sup>	Ag <sup>107</sup>	Cd <sup>111</sup>	Sn <sup>118</sup>	Sb <sup>121</sup>	Te <sup>125</sup>	Ba <sup>137</sup>	W <sup>182</sup>	Au <sup>197</sup>	Tl <sup>205</sup>	Pb <sup>208</sup>	Bi <sup>209</sup>	U <sup>238</sup>
Talga deposit, all sulfides (n = 14)																							
min	1.5	0.03	0.02	93	0.03	3	571	3	18	0.1	0.01	10	0.3	0.01	9	0.05	0.04	4.9	0.01	0.1	41	0.1	0.01
max	246	27	2.4	2422	1802	738	1.4 *	8.3 *	0.17 *	1.0	2.5	660	622	0.8	5394	103	33	58	0.17	13.1	10*	32.1	0.53
av	34.4	8.03	0.86	512	513	231	4606	0.7 *	729	0.41	0.56	214	52.3	0.21	829	28.0	6.32	25.0	0.05	4.11	1.3*	5.25	0.12
σ	42.6	8.26	0.68	515	516	230	4144	1.1 *	594	0.22	0.58	198	83.5	0.20	1038	30.0	6.10	10.9	0.05	3.81	1.7*	5.70	0.14
med	3.7	2.85	0.6	231	131	108	1539	82	614	0.30	0.15	117	4.0	0.10	185	9.5	2.7	24	0.02	2.05	0.3*	2.05	0.02
Dergamysh deposit, open-latticework pyrrhotite (Podg) (n = 11)																							
min	2.65	0.13	3.03	4.26	423	631	41	1.33	43	53	1.24	0.52	0.01	0.46	7.62	0.02	0.002	0.00	0.06	0.11	0.39	0.00	0.00
max	4.23	0.45	14	11	0.4 *	0.8 *	1.4 *	7.5	97	134	2.69	0.74	0.41	0.81	18	0.07	0.55	0.06	1.1	0.43	6.5	0.55	0.00
av	3.6	0.27	6.9	8.0	0.12 *	0.2 *	0.4 *	3.6	67.7	85.2	2.1	0.72	0.19	0.73	14.0	0.03	0.07	0.01	0.27	0.21	2.31	0.07	0.00
σ	0.26	0.08	3.0	1.68	702	0.12 *	0.4 *	1.59	16.0	21.4	0.36	0.05	0.11	0.1	2.62	0.01	0.1	0.01	0.24	0.08	1.67	0.09	0.00
med	3.24	0.25	5.4	7.28	873	990	64	2.84	53	77	1.93	0.66	0.13	0.66	12	0.02	0.001	0.01	0.09	0.14	1.21	0.00	0.00

Table 1. Cont.

Values	Ti <sup>49</sup>	V <sup>51</sup>	Cr <sup>53</sup>	Mn <sup>55</sup>	Co <sup>59</sup>	Ni <sup>60</sup>	Cu <sup>65</sup>	Zn <sup>66</sup>	As <sup>75</sup>	Se <sup>77</sup>	Mo <sup>95</sup>	Ag <sup>107</sup>	Cd <sup>111</sup>	Sn <sup>118</sup>	Sb <sup>121</sup>	Te <sup>125</sup>	Ba <sup>137</sup>	W <sup>182</sup>	Au <sup>197</sup>	Tl <sup>205</sup>	Pb <sup>208</sup>	Bi <sup>209</sup>	U <sup>238</sup>
Dergamysh deposit, coarse-crystalline pyrite (Pydg) (n = 37)																							
min	3.04	0.02	0.02	0.41	152	323	1	0.83	353	4.5	0.22	0.01	0.00	0.09	8.03	0.00	0.001	0.01	0.00	0.01	0.04	0.00	0.00
max	4.56	0.35	10	3.8	1293	1423	490	25	1603	99	1.06	0.17	0.16	0.17	71	0.04	0.05	0.31	0.28	0.43	1.45	0.05	0.01
av	3.7	0.08	1.90	1.48	639	758	161	3.5	873	33.3	0.56	0.05	0.05	0.13	41.83	0.01	0.01	0.03	0.03	0.14	0.32	0.01	0.00
$\sigma$	0.4	0.1	2.6	0.8	314	251	156	4.7	430	29.0	0.2	0.01	0.02	0.02	12.9	0.01	0.01	0.07	0.05	0.11	0.34	0.01	0.001
med	3.55	0.05	1.02	1.29	616	709	144	1.92	716	22	0.57	0.04	0.03	0.13	41	0.01	0.005	0.01	0.01	0.01	0.19	0.00	0.00
Dergamysh deposit, all sulfides (n = 48)																							
min	2.65	0.02	0.02	0.41	152	323	1	0.83	43	4.5	0.22	0.01	0.00	0.09	8.03	0.00	0.001	0.00	0.00	0.01	0.04	0.00	0.00
max	4.56	0.45	14	11	0.4 *	0.8 *	1.4 *	25	1603	134	2.69	0.74	0.41	0.81	71	0.07	0.55	0.06	1.1	0.43	6.5	0.55	0.01
av	3.61	0.12	3.04	2.8	759	962	873	3.46	687	44.0	0.87	0.19	0.07	0.25	35.2	0.03	0.02	0.01	0.08	0.15	0.73	0.02	0.00
$\sigma$	0.35	0.09	2.76	2.12	360	415	0.13 *	2.50	429	29.3	0.48	0.21	0.06	0.19	13.8	0.03	0.03	0.01	0.09	0.08	0.72	0.03	0.00
med	3.52	0.08	1.52	1.51	627	746	130	2.14	556	44	0.71	0.07	0.04	0.13	39.5	0.01	0.005	0.01	0.02	0.13	0.25	0.006	0.00

\*, wt. %; n, number of analyses; min, minimum; max, maximum; av, average;  $\sigma$ , standard deviation; med, median.

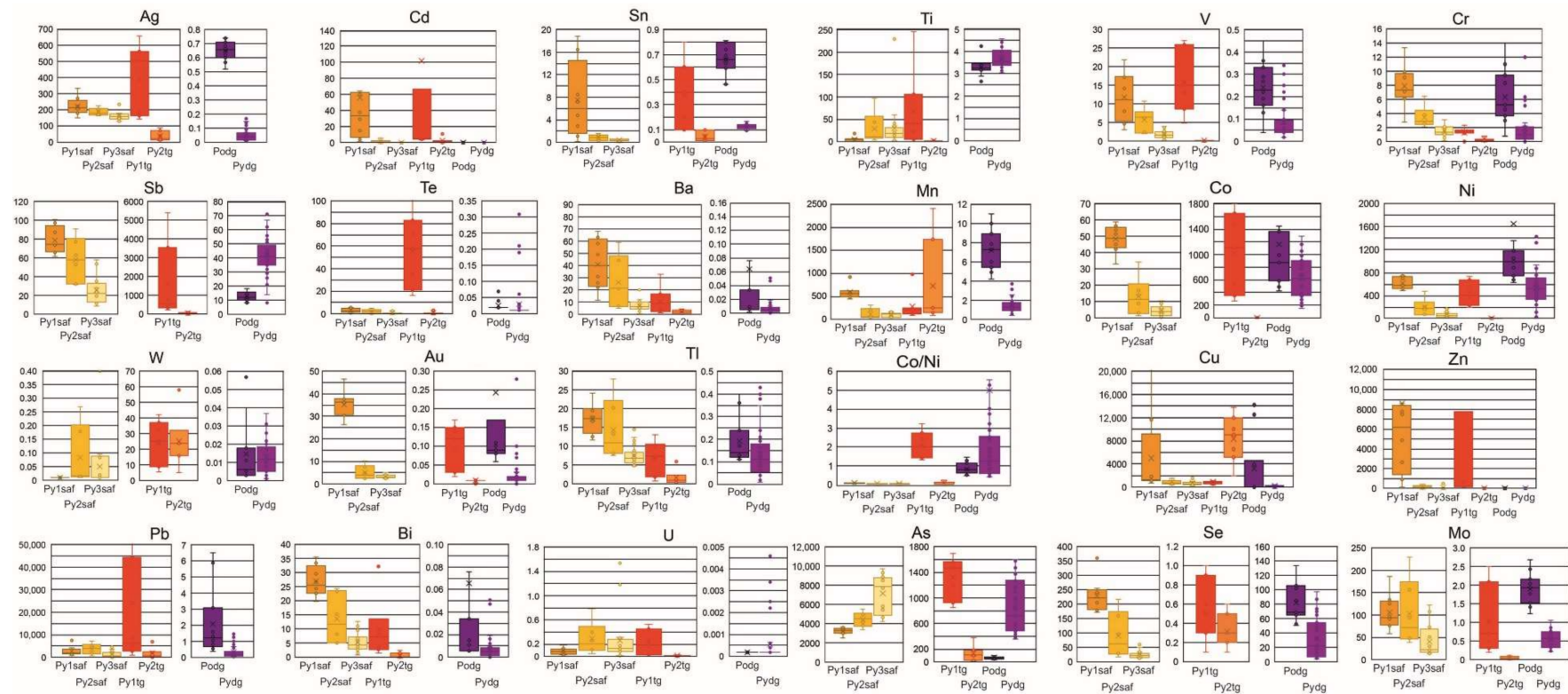


**Figure 6.** Box-and-whisker plots for trace elements in sulfides of nodules from sulfide–black shale diagenites of the Saf’yanovskoe deposit, sulfide–carbonate–hyaloclastite diagenites of the Talgan deposit, and sulfide–serpentinite diagenites of the Dergamysh deposit.

*As.* The extremely high As contents are determined in pyrite nodules from sulfide–black shale diagenites. They increase from the core to the rim in a range of fine-crystalline pyrite (Py1saf) (0.3 wt. %) → small-grained pyrite (Py2saf) (0.5 wt. %) → coarse-crystalline pyrite (Py3saf) (0.8 wt. %) (Figure 6). In contrast, in nodules from sulfide–carbonate–hyaloclastite diagenites, the As contents decrease from the core to the rim from 1468 ppm (Py1tg) to 112 ppm (Py2tg) (Figure 6). The lowest As contents are typical of nodules from sulfide–serpentinite diagenites, where As contents increase from the core to the rim similarly to the Saf’yanovskoe deposit: from 53 ppm in pyrrhotite (Podg) to 716 in coarse-crystalline pyrite (Pydg) (Figure 6).

*Se.* The fine-crystalline pyrite (Py1saf) from sulfide–black shale diagenites is mostly rich in Se (218 ppm) (Figure 6). The Se contents of pyrite of nodules from these diagenites decrease to the rim: 30.1 ppm in small-grained pyrite (Py2saf) and 21.4 ppm in coarse-crystalline pyrite (Py3saf). The coarse-crystalline pyrite (Pydg) from sulfide–serpentinite diagenites has similar low Se contents (22 ppm). The Se contents of pyrrhotite (Podg) from sulfide–serpentinite diagenites are slightly higher (77 ppm) (Figure 6). The lowest Se contents (0.3 ppm) are typical of pyrite from sulfide–carbonate–hyaloclastite diagenites.

*Mo.* The maximum Mo contents are detected in pyrite nodules from sulfide–black shale diagenites, where they decrease from the core to the rim in a range from fine-crystalline pyrite (Py1saf) (97 ppm) → small-grained pyrite (Py2saf) (49.1 ppm) → coarse-crystalline pyrite (Py3saf) (22 ppm) (Figure 6). The lowest Mo contents are typical of nodules both from sulfide–carbonate–hyaloclastite and sulfide–serpentinite diagenites.

*Au and Ag.* The highest Au contents are registered in pyrite nodules from sulfide–black shale diagenites, where they decrease from the core to the rim of the nodule from extremely high content of 36.2 ppm in fine-crystalline pyrite (Py1saf) to 3.25 ppm in small-grained pyrite (Py2saf) and 3.12 ppm in coarse-crystalline pyrite (Py3saf) (Figure 6). The Ag contents of pyrite of this nodule decrease in the same range from 206 to 176 and 159 ppm. In sulfide–carbonate–hyaloclastite diagenites, the Au and Ag contents in pyrite nodules behave similarly, decreasing from fine-grained pyrite (Py1tg) (0.12 and 504 ppm, respectively) to coarse-crystalline pyrite (Py2tg) (0.01 and 23.0 ppm, respectively). The lowest Au and Ag contents also decreasing from the core to the rim are detected in pyrite and pyrrhotite from sulfide–serpentinite diagenites.

*Sn.* All types of pyrite studied are characterized by low Sn contents (0.01–18.9 ppm). Their relatively higher contents are typical only of fine-crystalline pyrite (Py1saf) of sulfide–black shale diagenites.

*Sb.* The highest Sb contents (551 ppm) are detected in fine-grained pyrite (Py1tg) of sulfide–carbonate–hyaloclastite diagenites, which decrease to 58 ppm in coarse-crystalline pyrite (Py2tg). Similar decrease in Sb contents from the core to the rim in a range from fine-crystalline pyrite (Py1saf) (74.6 ppm) → small-grained pyrite (Py2saf) (52.9) → coarse-crystalline pyrite (Py3saf) (22.4 ppm) is typical of the pyrite nodule from sulfide–black shale diagenites (Figure 6). The lowest Sb contents are characterized for pyrite and pyrrhotite from sulfide–serpentinite diagenites.

*Pb, Te, and Bi.* The Pb contents of pyrite nodules from Saf’yanovskoe and Talgan deposits are correlated with Te and Bi contents. All pyrite types except for pyrite from sulfide–serpentinite diagenites exhibit wide variations and high Pb contents (Figure 6). The highest Te contents (58 ppm) and higher Bi contents (7.1 ppm) are typical of fine-grained pyrite (Py1tg) of sulfide–carbonate–hyaloclastite diagenites. The low Te (2.4 ppm) and higher Bi (24.3 ppm) contents are determined in fine-crystalline pyrite (Py1saf) of sulfide–black shale diagenites. The contents of these elements significantly decrease toward the rim of the nodule. The extremely low Te and Bi contents are characteristic of pyrite nodule from sulfide–serpentinite diagenites (Figure 6).

*Ba.* The Ba contents in all pyrite types vary (0.1–68 ppm), being extremely low (0.1 ppm) in sulfides from sulfide–black shale diagenites (Figure 6).

*W.* The high W contents (24 and 24 ppm) are detected in fine-grained (Py1tg) and coarse-crystalline (Py2tg) pyrite of sulfide–carbonate–hyaloclastite diagenites in contrast to low W contents in sulfides of nodules from both sulfide–black shale and sulfide–serpentinite diagenites (Figure 6).

*Tl*. The highest Tl contents (17.7 ppm) are detected in fine-crystalline pyrite (Py1saf) of sulfide–black shale diagenites, where they decrease toward the rim of the nodule (Figure 6). In pyrite nodule from sulfide–carbonate–hyaloclastite diagenites, the higher (7.4 ppm) and lower (0.9 ppm) Tl contents are characteristic of fine-grained (Py1tg) and subhedral coarse-crystalline (Py2tg) pyrite, respectively. The lowest Tl contents are determined in nodules from sulfide–serpentinite diagenites (Figure 6).

*U*. The U contents are generally low in all types of nodules being higher in a sulfide nodule from sulfide–black shale (0.08–0.15 ppm) and sulfide–carbonate–hyaloclastite (0.01–0.18 ppm) diagenites (Figure 6).

#### 4.3. Trace Element Correlations

Several trace elements exhibit good correlations (Figure 7). Most pyrite varieties are characterized by positive Co and Ni correlations excluding coarse-crystalline pyrite (Py2tg) from sulfide–carbonate–hyaloclastite and sulfide–serpentinite diagenites. The fine-crystalline pyrite (Py1saf) and small-grained pyrite (Py2saf) of sulfide–black shale diagenites and coarse-crystalline pyrite (Pydg) of sulfide–serpentinite diagenites has a positive correlation between Co and Tl ( $r = 0.87$  and  $0.91$ , respectively, and  $0.64$ ). The small-grained pyrite (Py2saf) and coarse-crystalline pyrite (Py3saf) of this nodule demonstrate a number of positively correlated trace element pairs, such as Tl–Sb ( $r = 0.92$  and  $0.87$ ), As–Se ( $r = 0.91$ ), Se and Pb ( $r = 0.82$ ), and Tl–Se ( $r = 0.89$  and  $0.86$ ) (hereinafter, one number indicates identical correlations in both pyrite types). These pyrite varieties are also characterized by negative correlations between Tl and As ( $r = -0.85$ ), As and Sb ( $r = -0.75$ ), and As and Se ( $r = -0.75$ ). The fine-grained pyrite (Py1tg) and coarse-crystalline pyrite (Py2tg) from sulfide–carbonate–hyaloclastite diagenites are remarkable for positive Tl–Ag correlation ( $r = 0.95$  and  $0.72$ , respectively). This pyrite is also characterized by positive Tl–Se correlation ( $r = 0.88$ ), whereas coarse-crystalline pyrite (Py2tg) shows a positive Tl–Mn correlation ( $r = 0.73$ ) and negative Cu–Sb correlation ( $r = -0.92$ ). The coarse-crystalline pyrite (Pydg) from sulfide–serpentinite diagenites exhibit a positive Tl–Sb correlation ( $r = 0.61$ ) and negative As–Se and Cu–As correlations ( $r = -0.60$  and  $0.62$ , respectively).

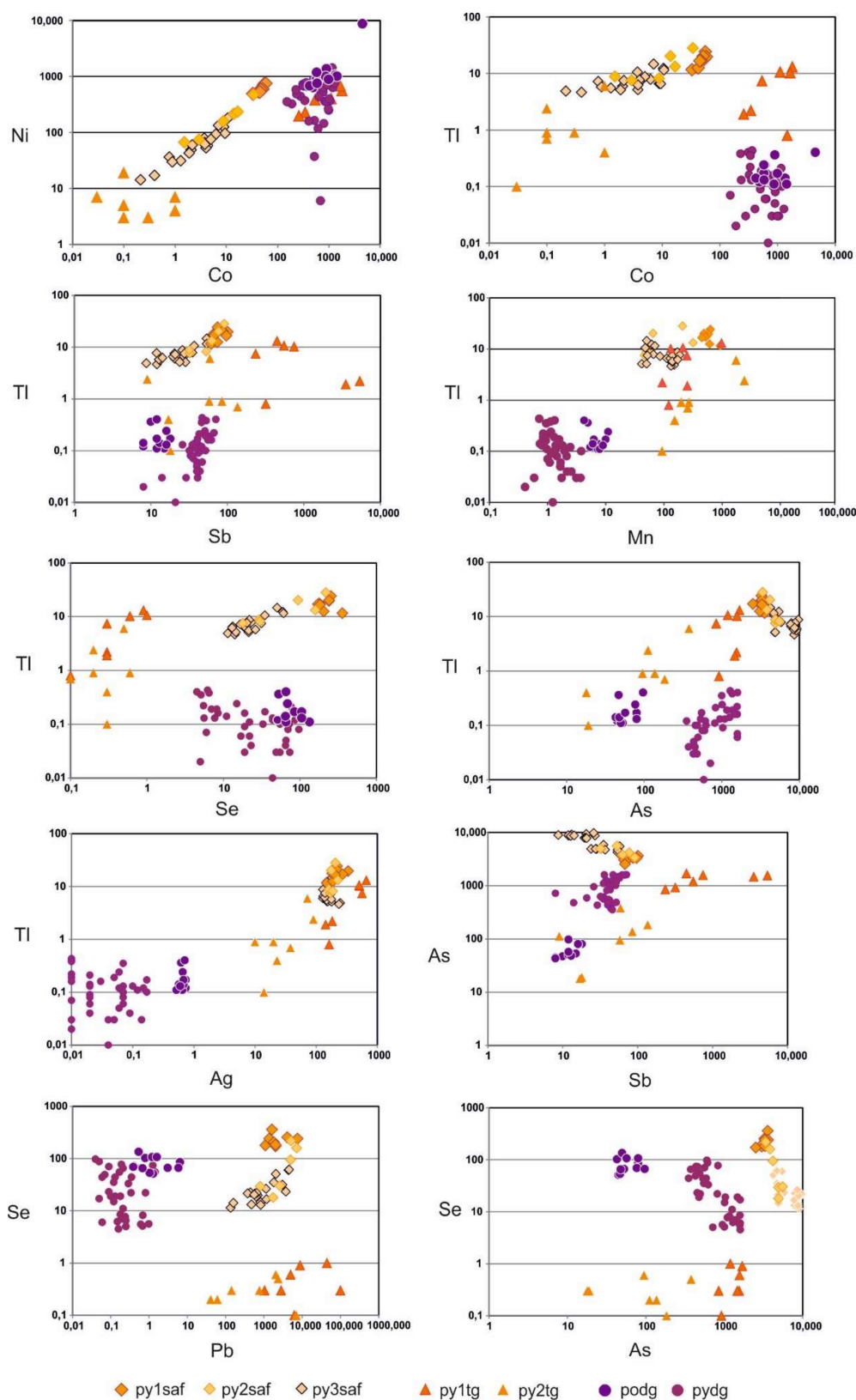


**Figure 7.** Correlation between selected trace elements in pyrite nodules of the Saf'yanovskoe (rhombs), Talgan (triangles), and Dergamysh (circles) deposits.

#### 4.4. Trace Element Zoning of Pyrite Nodules

LA-ICP-MS mapping of pyrite nodules from sulfide–black shale, sulfide–carbonate–hyaloclastite, and sulfide–serpentine diagenites have shown the zonal distribution of trace elements within the nodules (Figure 8). The core of the nodule from sulfide–black shale and sulfide–carbonate–hyaloclastite diagenites is enriched in Co, Ni, and Sb in contrast to the nodule from sulfide–serpentine diagenites, where Co, Ni, and Sb exhibit patchy enrichment of the rim. Arsenic behaves similarly in nodules from sulfide–black shale and sulfide–serpentine diagenites, where it is enriched in the rims. In nodules from sulfide–carbonate–hyaloclastite diagenites, As is concentrated in the core.

Lead is enriched in the intermediate zone and the core of nodules from sulfide–black shale and sulfide–carbonate–hyaloclastite diagenites, respectively, and has nonuniform distribution in the nodule from sulfide–serpentine diagenites. Copper exhibits higher contents mostly in the core of all three nodules, as well in the intermediate zone from sulfide–black shale diagenites.

In sulfide–black shale and sulfide–serpentine diagenites, Se accumulates in the core and the rim of the nodules, respectively, and has relatively even distribution in the nodule from sulfide–carbonate–hyaloclastite diagenites. Silver is confined to the core in the case of sulfide–carbonate–hyaloclastite diagenites, the intermediate zone and the rim in the case of sulfide–black shale diagenites, and is evenly distributed in the nodules from sulfide–serpentine diagenites. Thallium is enriched in the core and the intermediate zone of nodules from sulfide–carbonate–hyaloclastite and sulfide–black shale diagenites and is unevenly concentrated in the rim of the nodule from sulfide–serpentine diagenites.

The core of the nodule from sulfide–black shale diagenites is also enriched in Zn, Mn, Au, and Bi and the intermediate zone exhibits the higher contents of Mo (Figure 9) in contrast to nodules from sulfide–carbonate–hyaloclastite and sulfide–serpentine diagenites.

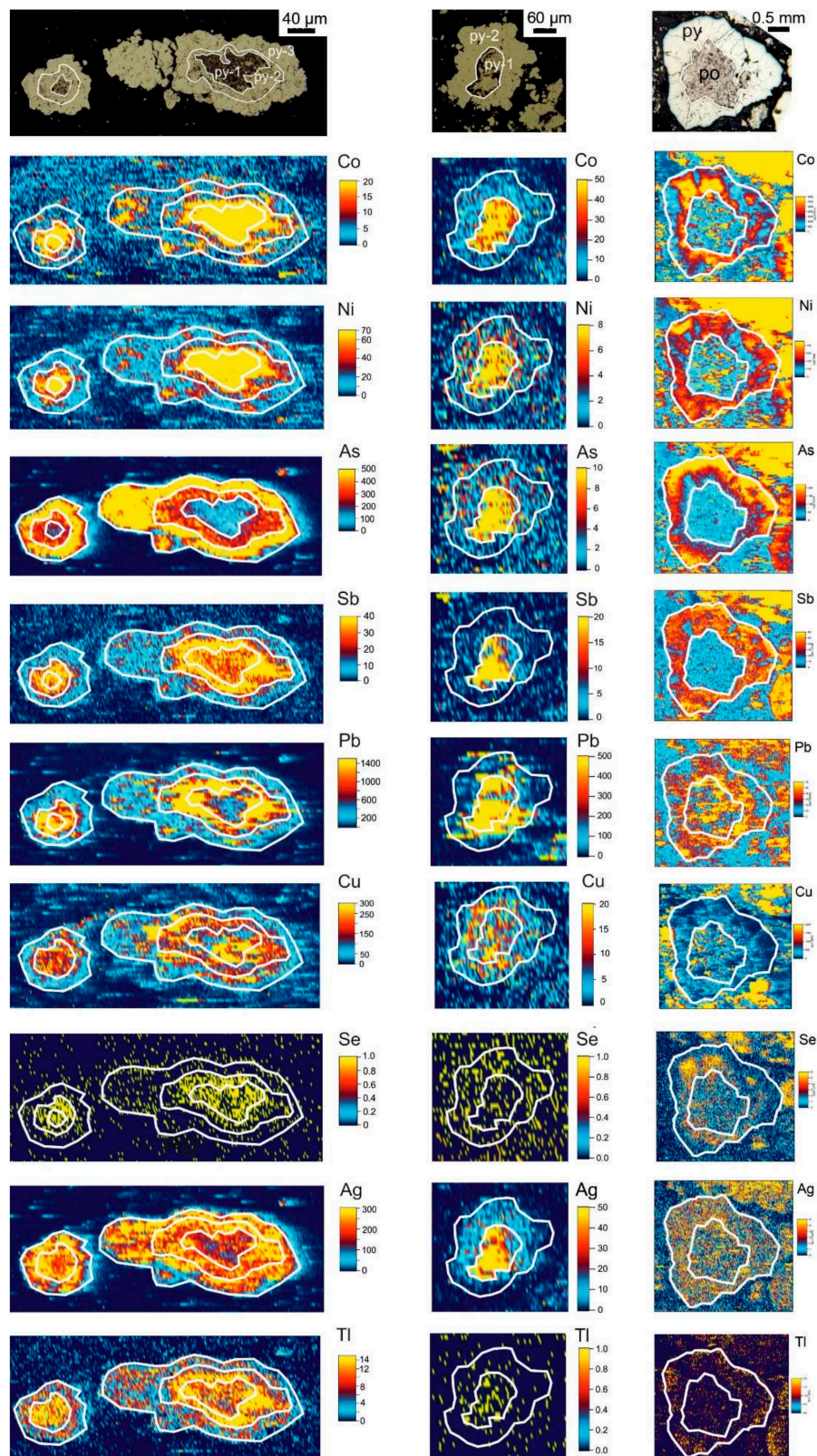


**Figure 8.** LA-ICP-MS pattern for selected trace elements of sulfide nodules from sulfide-black shale, sulfide-carbonate-hyaloclastite, and sulfide-serpentinite diagenites of the Saf'yanovskoe, Talgan, and Dergamysh deposits, respectively.

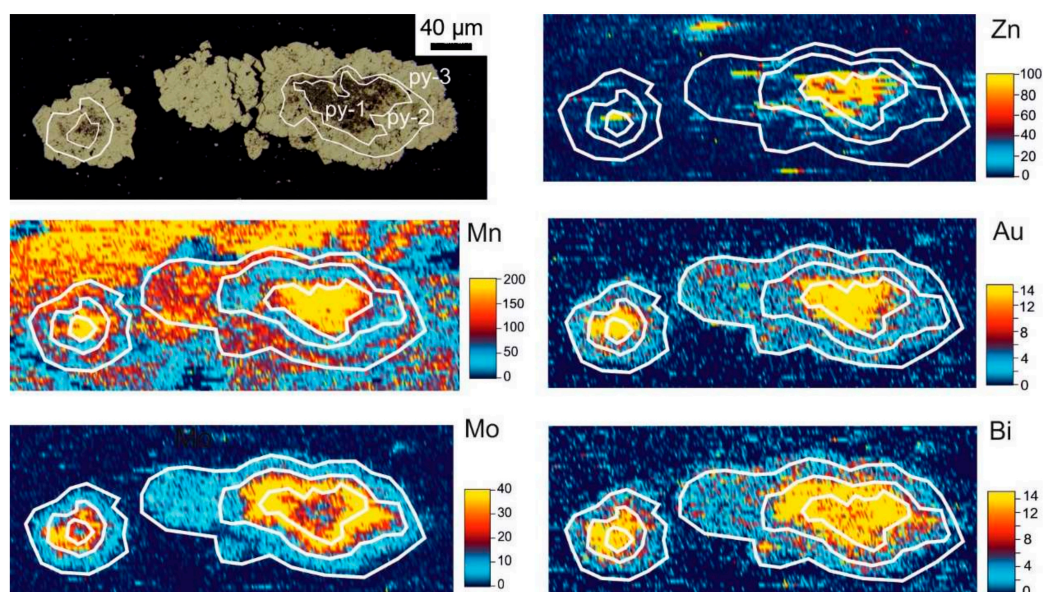


**Figure 9.** LA-ICP-MS pattern for Zn, Mn, Au, Mo, and Bi of sulfide nodule from sulfide–black shale diagenites of the Saf’yanovskoe deposit.

## 5. Discussion

Irrespective of the type of massive sulfide deposits (Rudny Altai, Uralian, or Atlantic), the diagenetic processes with formation of zoned pyrite nodules are similar in all the reviewed deposits. The zoned structure of pyrite nodules can shed light on specific stages and formation conditions of each zone and indicates that diagenetic and anadiagenetic conditions (cf., [48]) play important role in formation of accessory mineral assemblages and chemical composition of the nodules. The presence of various associated background sediments (black shales, hyaloclastites, carbonates, clastic serpentinites) is a key factor affecting the diversity of accessory authigenic minerals, which occur inside the pyrite nodules.

### 5.1. Morphology of Pyrite Nodules

The sulfide nodules from sulfide–black shale, sulfide–carbonate–hyaloclastite, and sulfide–serpentinite diagenites of the Saf’yanovskoe, Talgan, and Dergamysh deposits are characterized by a similar zoned structure with the core and the rim and are similarly replaced by authigenic minerals in the fine-crystalline (–grained) porous core. Similar morphological structures in massive sulfide deposits worldwide are poorly recognized (e.g., “pyrite blebs” in associated sedimentary rocks of the Brunswick 12 massive sulfide deposit [49]) or their formation is ascribed to hydrothermal or metamorphic processes (e.g., nodular pyrite in the Bracemac-McLeod (Canada) massive sulfide deposits [14]). In our cases, we believe in diagenetic origin of pyrite nodules, which is supported by the following features. The core of the nodules formed during early diagenesis, which is evident from the presence of associated framboidal pyrite (Saf’yanovskoe deposit) (Figure 3c), a typical product of early diagenesis of sedimentary rocks [50,51]. The formation of the intermediate zone and coarse-crystalline rim of the nodules is most likely related to late diagenetic processes. This is supported by anadiagenetic fractures cutting the nodules as a result of dehydration of sediments [52]. These fractures are filled with quartz, chlorite, illite, and calcite, which are late diagenetic–anadiagenetic transformation products of hyaloclastic material [53–57]. These fractures also host authigenic chalcopyrite and fahlores in the Saf’yanovskoe deposit and sphalerite, chalcopyrite, and galena in the Talgan deposit, which also replace the core of the nodules. According to these morphological data and the growth models of pyrite nodules recently suggested by [58], our nodules formed pervasively around numerous nucleation centers inside the background sediments with minor involvement of seawater and their formation

results in diagnostic trace element zonation. Nodules formed in this fashion also have relatively more matrix inclusions [58], which is also supported by our case.

The complete replacement of the core of the nodule by pyrrhotite in the Dergamysh deposit obscures the early diagenetic stage of the nodule's growth, however, similarly to the Saf'yanovskoe and Talgan deposits, it can be suggested that the core and the rim of the nodule from Dergamysh deposit formed also during early and late diagenesis, respectively. The rim of this nodule is also fractured by pyrrhotite veinlets, thus we believe in the anadiagenetic origin of pyrrhotite similarly to chalcopyrite, galena, fahlores, and arsenopyrite in the Saf'yanovskoe deposit and sphalerite, chalcopyrite, and galena in the Talgan deposit. The formation of different authigenic mineral assemblages of three deposits depends on the mineral composition of primary sulfide clasts and background sediments (see also below).

### 5.2. Geochemistry of Pyrite Nodules

The core of all studied nodules, as a rule, is enriched in trace elements relative to other zones (Figure 10a–c) similarly to that of pyrite nodules from the Lahanos (Turkey) and Bracemac–McLeod (Canada) massive sulfide [14,15] and numerous gold [3,11] deposits. This is explained by two main reasons: (i) precipitation of the core from diagenetic fluids rich in trace elements due to dissolution of primary hydrothermal pyrite and sphalerite–chalcopyrite–pyrite clasts with inclusions of hydrothermal galena, tellurides, fahlores, and other accessory ore minerals and (ii) fast low-temperature growth of nodular cores, which allows the trace elements to be incorporated into pyrite in solid solution or as small inclusions [2]. The cores of our nodules can contain both syngenetic (early diagenetic) and epigenetic (late diagenetic) inclusions of ore minerals, which is suggested from different trace element correlations. In particular, Py1saf from the Saf'yanovskoe nodule has no Pb–Se correlation in contrast to positive Pb and Se correlation in Py2saf and Py3saf. This most likely indicates the presence of two different generations of authigenic galena (Se-free and Se-bearing) in sulfide nodules. The enrichment of Py1saf in trace elements relative to Py2saf and Py3saf (as well as the enrichment of Py2saf in trace elements relative to Py3saf) is also evident from median elemental ratios for each pyrite type normalized to total median elemental ratios (Table 2).

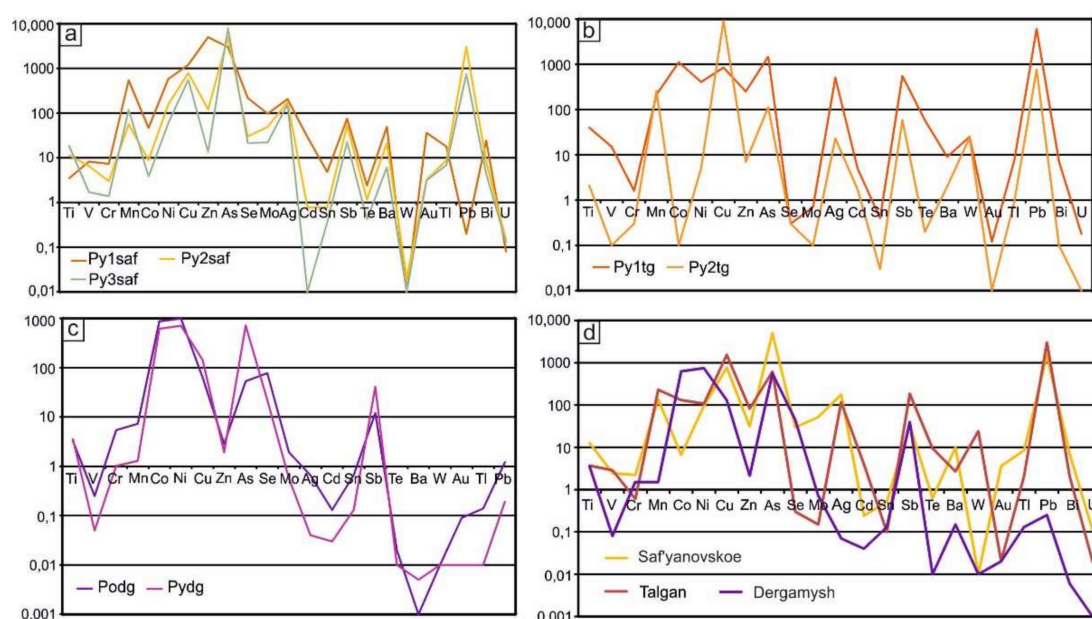


**Figure 10.** Comparative log–log plots for median trace element composition of individual zones of sulfide nodules from sulfide–black shale diagenites of the Saf'yanovskoe deposit (a), sulfide–carbonate–hyaloclastite diagenites of the Talgan deposit (b), sulfide–serpentinite diagenites of the Dergamysh deposit (c), and their general trace element composition including all zones of each nodule (d).

**Table 2.** Range of accumulation of trace elements in pyrite nodule from the Saf'yanovskoe massive sulfide deposit ( $\text{median}_{\text{element}}/\text{median}_{\text{all sulfides}}$ ).

Pyrite Types	Zn	Cd	Au	Sn	Se	Co	Ni	Ba	Mn	Te	Bi	V
Py1saf	156.4	120.8	10.1	9.41	7.34	6.99	6.15	4.92	3.98	3.84	3.47	3.37
	<b>Zn</b>	<b>Cd</b>	<b>V</b>	<b>Ba</b>	<b>W</b>	<b>Pb</b>	<b>Te</b>	<b>Ni</b>	<b>Sb</b>	<b>Sn</b>	<b>Cr</b>	<b>U</b>
Py2saf	3.88	3.21	2.69	2.13	2.00	1.99	1.87	1.67	1.57	1.53	1.35	1.32
	<b>As</b>	<b>Ti</b>	<b>U</b>	<b>W</b>	<b>Ag</b>	<b>Mn</b>	<b>Au</b>	<b>Tl</b>	<b>Cu</b>	<b>Se</b>	<b>Sn</b>	<b>V</b>
Py3saf	1.61	1.45	1.11	1.00	0.91	0.88	0.87	0.82	0.73	0.72	0.71	0.70
	<b>Cr</b>	<b>Sb</b>	<b>Tl</b>	<b>Mo</b>	<b>Cu</b>	<b>Pb</b>	<b>Ag</b>	<b>W</b>	<b>U</b>	<b>As</b>	<b>Ti</b>	
Py1saf	3.30	2.22	2.1	1.87	1.65	1.34	1.17	1.00	0.70	0.67	0.28	
	<b>Co</b>	<b>Bi</b>	<b>Tl</b>	<b>Cu</b>	<b>As</b>	<b>Se</b>	<b>Ag</b>	<b>Mo</b>	<b>Au</b>	<b>Ti</b>	<b>Mn</b>	
Py2saf	1.20	1.16	1.04	1.03	1.02	1.01	1.00	0.95	0.91	0.90	0.41	
	<b>Sb</b>	<b>Te</b>	<b>Ni</b>	<b>Cr</b>	<b>Bi</b>	<b>Ba</b>	<b>Co</b>	<b>Pb</b>	<b>Zn</b>	<b>Mo</b>	<b>Cd</b>	
Py3saf	0.67	0.67	0.64	0.62	0.62	0.61	0.57	0.50	0.43	0.43	0.04	

The values of >1 and <1 indicate the enrichment and depletion of trace elements relative to the median values for all pyrite types, respectively.

The crystalline pyrite of the rims of the nodules is mostly depleted in trace elements (Table 3), first, due to depletion of late diagenetic pore fluids in trace elements and, second, its slower crystallization at relatively higher temperatures, which allowed the trace elements to be partitioned into separate mineral phases, which form much larger inclusions in comparison with early pyrite [2]. The pyrite nodules from other massive sulfide and gold deposits also contain the intermediate zone, which can either be depleted (Lahanos [15], gold deposits of Spain [2]) or enriched (Saf'yanovskoe (our data) and Bracemac–McLeod deposits [14]) in trace elements. Late diagenetic pyrite (rim) of the nodules of massive sulfide and gold deposits is mostly depleted in trace elements except for some outbursts related to inclusions of accessory minerals (galena, fahlore, arsenopyrite, native gold, cobaltite, tellurides). The duration of early and late diagenesis processes can be estimated from the age of sulfide breccias with pyrite nodules from the Semenov-3 hydrothermal field in the Mid-Atlantic Ridge [17], the age of which varies from 35.5 to 90.3 kyr [59].

**Table 3.** Trace element associations in pyrite nodules of the Saf'yanovskoe, Talgan, and Dergamysh deposits.

Saf'yanovskoe Deposit, all sulfides (n = 33)
I (Cd + Zn + Sn) + II (Co + Ni + Bi + Sb + Mo + Tl + Pb + Te) + III (Ba + V + Cr) + IV (Se + Au + Mn) + V (Cu + Ag) + VI (U + W) Ti, As
Talgan deposit, all sulfides (n = 14)
I (Cd + Zn + Ba) + II (V + U + Cr) + III (Ni + Co) + IV (Te + Ag + Au + Tl + Se) V (Pb + Bi) + VI (Sn + Ti) VII (Mo + Sb + As) VIII (Cu + Mn) W
Dergamysh deposit, all sulfides (n = 47)
I (Ni + Bi) + II (Ba + Au + Pb) + III (Ag + Sn) + IV (Mo + Mn) + V (V + Cr + Cu + Tl) VI (As + Sb + Ti) VII (U + Zn) VIII (Co + Se) IX (W + Cd)

Pluses mean correlations between associations. For correlation matrices, see Supplementary Material.

The influence of background sediments (black shales, hyaloclastites, carbonates, clastic serpentinites) is evident from general trace element composition of the nodules (Figure 10d). The nodule from sulfide–black shale diagenites of the Saf'yanovskoe deposit accumulates most trace elements including Ti, V, Cr, As, Se, Mo, Ag, Sn, Ba, Au, Tl, Bi, and U. It is commonly accepted that organic-rich sediments provide favorable anoxic conditions for the accumulation of a wide spectrum of trace elements [49,60], including Mo, As, V, and U, which are easily scavenged from seawater by

organic matter [60]. Molybdenum and V are considered especially important elements for ancient organic-rich sediments [60] and, in the Saf'yanovskoe case, their possible relation to associated black shales is reflected in positive Mo–V correlation in Py1saf (0.58, Supplementary Material). Similar enrichment of early diagenetic pyrite in trace elements (including Mo, Ba, Se, Ag, Cr, U, and V) is observed in orogenic black shale-hosted gold deposits [1–4]. The enrichment of massive sulfides in As, Mo, Sn, Au, Tl, and Bi resulting in formation of various As-, Mo-, Sn-, Au-, Tl-, and Bi-bearing minerals is also typical of continental massive sulfide deposits and seafloor hydrothermal sulfide fields associated with organic-rich sediments [24,61,62].

The nodule from sulfide–carbonate–hyaloclastite diagenites of the Talgan deposit is rich in V, Mn, Cu, Zn, Cd, Sb, Te, W, and Pb, which were sourced from seawater (V), hyaloclastites (Mn, W), and Cu–Zn ore clasts with numerous inclusions of accessory Te-, Pb-, and Sb-bearing minerals (Cu, Zn, Cd, Te, Pb). In contrast to the Saf'yanovskoe nodule, V in the Talgan pyrite nodule was not consumed by organic matter and was absorbed directly from seawater by clay minerals included in pyrite [63], which is supported by a positive correlation ( $r = 0.87$ , Supplementary Material) between V and U (typical seawater-derived elements [60,64]) in pyrite. The formation of abundant authigenic sphalerite occurred in higher alkaline conditions because of the presence of carbonate material (cf. [25]). In comparison with previously studied pyrite nodule with clear zoning [44], the pyrite nodule from this study exhibits much lower trace element contents. However, the core fine-grained pyrite (which is locally replaced by coarse-grained pyrite) remains rich in trace elements relative to the outer coarse-crystalline pyrite zone similarly to the nodule from [44].

Relative to the Saf'yanovskoe and Talgan examples, the nodule from sulfide–serpentinite diagenites of the Dergamysh deposit is rich in Co and Ni, which are typical trace elements of ultramafic rocks and primary ores from the deposit [27]. The formation of pyrrhotite after the core of the nodule occurred in reducing conditions provided by ultramafic clasts. High Co/Ni ratio ( $>1$ , Figure 6) of pyrite from the rim most likely indicates higher temperature of its deposition, which was also favorable for the formation of late authigenic Co, Ni, As, Bi, and Au minerals.

### 5.3. Mode of Occurrence of Trace Elements in Pyrite Nodules

The correlation analysis of trace elements, which are ranged from maximum to minimum correlation coefficients, is an effective tool for the identification of the mode of occurrence of trace elements in minerals [65]. Several trace element associations were identified for pyrite nodules of the deposits studied (Table 3).

The nodule of the Saf'yanovskoe deposit is characterized by six trace element associations (Table 3). Association I corresponds to Sn- and Cd-bearing sphalerite, which was found in the core of the nodule. Association II is partly related to isomorphic substitution and mineral inclusions. Most significant correlation coefficients were calculated for Co and Ni ( $r = 0.96$ ), Tl and Mo ( $r = 0.89$ ), Sb and Mo ( $r = 0.87$ ) (Supplementary Material, Figure 7), which occur as isomorphic substitutions in pyrite. The Pb + Te indicates the presence of galena and altaite inclusions found in the intermediate zone B. Galena can contain Se, which is indicated from correlation between Pb and Se ( $r = 0.82$ , Supplementary Material, Figure 7).

The associations III and VI are related to the inclusions of nonsulfidic minerals in the core (quartz, chlorite, illite, mica) and the rim (quartz, rutile, monazite, Ba-bearing mica). Association IV with strong correlation between Au, Se, and Mn is rather unusual, but it reflects the high contents of these trace elements in the core of the nodule (Figures 8 and 9). Enrichment in Mn is inherited from framboidal pyrite, which typically contains Mn [66,67] similarly to colloform pyrite suggesting its growing of pyrite under relatively oxygenated subalkaline conditions of seawater [13]. The Au and Se are most likely present as nanoparticles [10]. Association V with Cu and Ag indicates the occurrence of Ag-bearing chalcopyrite in the intermediate zone B.

Arsenic can be hosted in pyrite as nonstoichiometric substitutions [68] or can occur as ultramicroscopic inclusions assuming the presence of As-bearing minerals in the nodules. In the case

of the Saf'yanovskoe deposit, part of As (<5300 ppm, which is the maximum equilibrium solubility of As in pyrite at 600 °C [69]) occurs as coupled substitution along with Tl, which is supported from negative As–Tl correlation ( $r = -0.85$ ) (Supplementary Material, Figure 7). Incorporation of As and Tl into the structure of pyrite is another piece of evidence of slow growth of this pyrite type [68]. At the same time, the negative correlation between As and Sb ( $r = -0.75$ ), extremely high As contents, and low Sb (<100 ppm) contents are evidence of arsenopyrite inclusions, which were found in crystalline pyrite, rather than fahlore inclusions [68].

Titanium, which exhibits no correlations with other elements, reflects the presence of rutile inclusions in the nodule.

The nodule of the Talgan deposit is characterized by eight trace element associations (Table 3). Associations I and II indicate the presence of inclusions of sphalerite, barite, and non-opaque minerals (chlorite and illite) typical of the core of the nodule. Association III reflects typical isomorphic trace elements of pyrite [68]. The Tl- and Se-bearing gold-telluride mineral assemblage is incorporated in association IV. The presence of association V with Pb and Bi similar to that of the Saf'yanovskoe deposit is part of Bi-bearing galena from the core of the nodule. Association VI with Sn and Ti is related to the presence of cassiterite and rutile in the rim of the nodule. In contrast to the Saf'yanovskoe deposit, the association VII with correlated As, Sb, and Mo most likely indicates the presence of Mo-bearing (?) fahlore inclusions due to high contents of As and Sb [67]. Tungsten has no correlations with other elements, since it occurs as scheelite inclusions in the core of the nodule.

The pyrite nodule from the Dergamysh deposit is characterized by nine trace element associations (Table 3), which mostly reflect the inclusions of various minerals, such as Ni (nickeline) and Bi (pilsenite) minerals (association I), gold and unrecognized yet galena (association II), an unidentified Ag–Sn mineral (association III), silicates, which host Mo and Mn (association IV), and chromite and chalcopyrite (association V). The association VI contains typical elements of Sb-bearing sulfoarsenides (up to 2.28 wt. % Sb according to microprobe analyses [40]) and Ti-bearing silicate. Zinc is evident of sphalerite inclusions and is related to U (association VII) indicating involvement of seawater during formation of sphalerite, because it is considered that U is a typical “seawater”-derived element [64]. Association VIII most likely reflects isomorphic elements. The uncommon association of W and Cd (IX) can indicate microscopic inclusions of Fe oxides, which easily incorporate these elements into their structure [70–72].

## 6. Conclusions

The sulfide nodules of massive sulfide deposits studied are typical not only of sulfide–black shales diagenites of the Rudny Altai-type Saf'yanovskoe deposit, but also of sulfide–hyaloclastite–carbonate (Uralian-type Talgan deposit) and sulfide–serpentinite (Atlantic-type Dergamysh deposit) diagenites. All sulfide nodules are characterized by similar morphology and zoned structure with the core made up of porous fine-crystalline or fine-grained pyrite and the rim composed of crystalline pyrite. The core of the nodules is early diagenetic, whereas crystalline domains are late diagenetic. All nodules underwent anadiagenetic fracturing and replacement by authigenic sphalerite, chalcopyrite, galena, and fahlores in the Saf'yanovskoe deposit, sphalerite, chalcopyrite, and galena in the Talgan deposit, and pyrrhotite, chalcopyrite, and cubanite in the Dergamysh deposit.

The sulfide nodules from these deposits exhibit specific accessory mineral assemblages with dominant galena and fahlores in sulfide–black shales diagenites of the Saf'yanovskoe deposit, various tellurides of sulfide–hyaloclastite–carbonate diagenites of the Talgan deposit, and Co–Ni sulfoarsenides in sulfide–serpentinite diagenites of the Dergamysh deposit.

The important role in the formation of authigenic mineral assemblages and accumulation of trace elements is played by mineral composition of clastic massive sulfide ores mixed with background sediments. The sulfide nodules from sulfide–black shale diagenites of the Saf'yanovskoe deposit are enriched in most trace elements due to anoxic reducing conditions and effective sorption of trace elements by associated organic-rich sediments. The nodules from sulfide–carbonate–hyaloclastite

diagenites of the Talgan deposit are rich in elements, which were sourced from seawater, hyaloclastites and copper–zinc ore clasts with numerous inclusions of accessory Te-, Pb-, and Sb-bearing minerals. The sulfide nodules from sulfide–serpentinite diagenites of the Dergamysh deposit are rich in Co and Ni, which are typical trace elements of ultramafic rocks and primary ores from the deposit.

The cores of all studied nodules, as a rule, are enriched in trace elements relative to other zones, which is explained by its precipitation from diagenetic fluids rich in trace elements because of the dissolution of unstable primary hydrothermal ore clasts mixed with background sediments and fast growth allowing trace elements to be incorporated either as solid solutions or small inclusions. The crystalline pyrite of the rims of the nodules is mostly depleted in trace elements due to depletion of late diagenetic pore fluids in trace elements and its slower crystallization at relatively higher temperatures, which allowed the trace elements to be partitioned into larger mineral inclusions. The finding of ultramicroscopic inclusions or isomorphic substitutions of elements are highly supported by correlation analysis, which can be an effective tool for predicting the mode of occurrence of trace elements in minerals.

Our data significantly expand the knowledge on behavior of trace elements and formation of authigenic mineralization in massive sulfide deposits, which is especially important during forecast works, since the contents of trace elements in authigenic pyrite from associated volcanosedimentary horizons of massive sulfide deposit are one to two orders of magnitude higher than those from barren background sediments.

**Supplementary Materials:** The following are available online at <http://www.mdpi.com/2075-163X/10/2/193/s1>, Table S1: Trace element composition of pyrite nodules according to LA-ICP-MS analyses and correlation matrices for pyrite and pyrrhotite.

**Author Contributions:** Conceptualization, study of nodules from the Saf'yanovskoe deposit, original draft preparation, N.P.S.; study of nodules from the Dergamysh deposit, original draft preparation, review and editing, I.Y.M.; study of nodules from the Talgan deposit, original draft preparation, N.R.A.; LA-ICP-MS analyses, supervision, funding acquisition, review and editing, V.V.M.; LA-ICP-MS analyses, S.P.M.; LA-ICP-MS mapping, D.A.A.; SEM identification of mineral inclusions, I.A.B. All authors have read and agreed to the published version of the manuscript.

**Funding:** This research was funded by Russian Foundation for Basic Research (project no. 17-05-00854) and partly by the Ministry of Science and Higher Education (State Contract no. AAAA-A19-119061790049-3).

**Acknowledgments:** The authors are grateful to Ross Large and Leonid Danyushevsky (University of Tasmania) for help in LA-ICP-MS analysis of the Talgan nodule and Aleksandr Tseluyko (IMin) for help in figure preparation.

**Conflicts of Interest:** The authors declare no conflict of interest.

## References

1. Large, R.R.; Maslennikov, V.V.; Robert, F.; Danyushevsky, L.V. Multistage sedimentary and metamorphic origin of pyrite and gold in the giant Sukhoi log deposit, Lena Gold Province, Russia. *Econ. Geol.* **2007**, *102*, 1233–1267. [[CrossRef](#)]
2. Large, R.R.; Danyushevsky, L.; Hollit, H.; Maslennikov, V.V.; Meffre, S.; Gilbert, S.; Bull, S.; Scott, R.; Emsbo, P.; Thomas, H.; et al. Gold and trace element zonation in pyrite using a laser imaging technique: Implications for the timing of gold in orogenic and Carlin-style sediment-hosted deposits. *Econ. Geol.* **2009**, *104*, 635–668. [[CrossRef](#)]
3. Large, R.R.; Bull, S.W.; Maslennikov, V.V. A carbonaceous sedimentary source-rock model for Carlin-type and orogenic gold deposits. *Econ. Geol.* **2011**, *106*, 331–358. [[CrossRef](#)]
4. Gregory, D.D.; Large, R.R.; Halpin, J.A.; Baturina, L.E.; Lyons, T.W.; Wu, S.; Danyushevsky, L.; Sack, P.J.; Chappaz, A.; Maslennikov, V.V.; et al. Trace element content of sedimentary pyrite in black shales. *Econ. Geol.* **2015**, *110*, 1389–1410. [[CrossRef](#)]
5. Schoonen, M.A.A. Mechanisms of sedimentary pyrite formation. *GSA Spec. Pap.* **2004**, *379*, 117–134. [[CrossRef](#)]
6. Butler, I.B.; Rickard, D. Framboidal pyrite formation via the oxidation of iron (II) monosulfide by hydrogen sulphide. *Geochim. Cosmochim. Acta* **2000**, *64*, 2665–2672. [[CrossRef](#)]

7. Rickard, D. *Sulfidic Sediments and Sedimentary Rocks: Developments in Sedimentology*; Elsevier: Amsterdam, The Netherlands, 2012; Volume 65, 801p.
8. Large, R.R.; Halpin, J.A.; Danyushevsky, L.V.; Maslennikov, V.V.; Bull, S.W.; Long, J.A.; Gregory, D.D.; Lounejeva, E.; Lyons, T.W.; Sack, P.J.; et al. Trace element content of sedimentary pyrite as a new proxy for deep-time ocean-atmosphere evolution. *Earth Planet. Sci. Lett.* **2014**, *389*, 209–220. [[CrossRef](#)]
9. Huerta-Diaz, M.A.; Morse, J.W. Pyritization of trace metals in anoxic marine sediments. *Geochim. Cosmochim. Acta* **1992**, *56*, 2681–2702. [[CrossRef](#)]
10. Deditius, A.P.; Utsunomiya, S.; Reich, M.; Kesler, S.E.; Ewing, R.C.; Hough, R.; Walshe, J. Trace metal nanoparticles in pyrite. *Ore Geol. Rev.* **2011**, *42*, 32–46. [[CrossRef](#)]
11. Thomas, H.V.; Large, R.R.; Bull, S.W.; Maslennikov, V.V.; Berry, R.F.; Fraser, R.; Froud, S.; Moye, R. Pyrite and pyrrhotite textures and composition in Sedimentary rocks, laminated quartz veins, and gold reefs, at Bendigo Mine, Australia: Insights for ore genesis. *Econ. Geol.* **2011**, *105*, 1–40. [[CrossRef](#)]
12. Gregory, D.D.; Meffre, S.; Large, R.R. Comparison of metal enrichment in pyrite framboids from a metal-enriched and metal-poor estuary. *Am. Miner.* **2014**, *99*, 633–644. [[CrossRef](#)]
13. Maslennikov, V.V.; Ayupova, N.R.; Safina, N.P.; Tseluyko, A.S.; Melekestseva, I.Y.; Large, R.R.; Herrington, R.J.; Kotlyarov, V.A.; Blinov, I.A.; Maslennikova, S.P.; et al. Mineralogical features of ore diagenites in the Urals massive sulfide deposits, Russia. *Minerals* **2019**, *3*, 150. [[CrossRef](#)]
14. Genna, D.; Gaboury, D. Deciphering the hydrothermal evolution of a VMS system by LA-ICP-MS using trace elements in pyrite: An example from the Bracemac-McLeod deposits, Abitibi, Canada, and implication for exploration. *Econ. Geol.* **2015**, *110*, 2087–2108. [[CrossRef](#)]
15. Maslennikov, V.V.; Ayupova, N.R.; Artemyev, D.A.; Tseluyko, A.S. Microtopochemistry of marcazite pyrite nodule in illit-hematite gossanites of Lahanos massive sulfide deposit (Pontides, Turkey) by LAICP-MS data. *Mineralogiya* **2017**, *3*, 48–70. (In Russian)
16. Tseluyko, A.S.; Maslennikov, V.V.; Artem'yev, D.A. Microtopochemistry of pyrite nodules of siliceous siltstones from the Yubileinoe massive sulfide deposit (the Southern Urals) according to LA-ICP-MS data. *Litosfera* **2018**, *4*, 621–641. (In Russian)
17. Melekestseva, I.Y.; Maslennikov, V.V.; Safina, N.P.; Nimis, P.; Maslennikova, S.P.; Beltenev, V.; Rozhdestvenskaya, I.; Danyushevsky, L.; Large, R.; Artemyev, D.A.; et al. Sulfide breccias from the Semenov-3 hydrothermal field, Mid-Atlantic Ridge: Authigenic mineral formation and trace element pattern. *Minerals* **2018**, *8*, 321. [[CrossRef](#)]
18. Prokin, V.A.; Buslaev, F.P. Massive copper-zinc sulfide deposits in the Urals. *Ore Geol. Rev.* **1999**, *14*, 1–69. [[CrossRef](#)]
19. Puchkov, V.N. Structure and geodynamics of the Uralian orogen. *Geol. Soc. Spec. Publ.* **1997**, *121*, 201–236. [[CrossRef](#)]
20. Herrington, R.J.; Maslennikov, V.V.; Zaykov, V.V.; Seravkin, I.B.; Kosarev, A.S.; Bushmann, B.; Orgeval, J.-J.; Holland, N.; Tessalina, S.G.; Nimis, P.; et al. Classification of VHMS deposits: Lessons from the Uralides. *Ore Geol. Rev.* **2005**, *27*, 203–237. [[CrossRef](#)]
21. Puchkov, V.N. Ural tectonics: Modern views. *Geotektonika* **1997**, *4*, 42–60. (In Russian)
22. Puchkov, V.N. Relationship between plitotectonic and plume processes. *Geotectonics* **2016**, *4*, 425–438. [[CrossRef](#)]
23. Zaykov, V.V.; Maslennikov, V.V.; Zaykova, E.V.; Herrington, R. *Ore-Formational and Ore-Facies Analysis of Massive Sulfide Deposits of Ural Paleo-Ocean*; Imin UB RAS: Miass, Russia, 2001; 315p. (In Russian)
24. Maslennikov, V.V.; Maslennikova, S.P.; Ayupova, N.R.; Zaykov, V.V.; Tseluyko, A.S.; Melekestseva, I.Y.; Large, R.R.; Danyushevsky, L.V.; Herrington, R.J.; Lein, A.T.; et al. Chimneys in Paleozoic massive sulfide mounds of the Urals VMS deposits: Mineral and trace element comparison with modern black, grey, white and clear smokers. *Ore Geol. Rev.* **2017**, *85*, 64–106. [[CrossRef](#)]
25. Maslennikov, V.V.; Ayupova, N.R.; Maslennikova, S.P.; Tret'yakov, G.A.; Melekestseva, I.Y.; Safina, N.P.; Belogub, E.V.; Large, R.R.; Danyushevsky, L.V.; Tseluyko, A.S.; et al. *Toxic Elements in Massive Sulfide Systems*; Rio UB RAS: Yekaterinburg, Russia, 2014; 340p. (In Russian)
26. Maslennikov, V.V. *Lithogenesis and Formation of Massive Sulfide Deposits*; Imin UB RAS: Miass, Russia, 2006; 384p. (In Russian)

27. Melekestseva, I.Y.; Zaykov, V.V.; Nimis, P.; Tret'yakov, G.A.; Tessalina, S.G. Cu-(Ni-Co-Au)-bearing massive sulfide deposits associated with mafic-ultramafic rocks of the main Urals fault, South Urals: Geological structures, ore textural and mineralogical features, comparison with modern analogs. *Ore Geol. Rev.* **2013**, *52*, 18–37. [[CrossRef](#)]
28. Safina, N.P.; Melekestseva, I.Y.; Nimis, P.; Ankusheva, N.N.; Yuminov, A.M.; Kotlyarov, V.A.; Sadykov, S.A. Barite from the Saf'yanovka VMS deposit (Central Urals) and Semenov-1 and Semenov-3 hydrothermal sulfide fields (Mid-Atlantic Ridge): A comparative analysis of formation conditions. *Miner. Depos.* **2016**, *54*, 491–507. [[CrossRef](#)]
29. Maslennikov, V.V.; Melekestseva, I.Y.; Maslennikova, S.P.; Maslennikova, A.V.; Tret'yakov, G.A.; Ayupova, N.R.; Safina, N.P.; Filippova, K.A.; Udachin, V.N.; Aminov, P.G.; et al. *Differentiation of Toxic Elements in Lithogenesis and Technogenesis of Massive Sulfide Deposits*; Rio UB RAS: Yekaterinburg, Russia, 2016; 368p. (In Russian)
30. Ayupova, N.R.; Maslennikov, V.V.; Tessalina, S.G.; Shilovsky, O.P.; Sadykov, S.A.; Hollis, S.P.; Danyushevsky, L.V.; Safina, N.P.; Statsenko, E.O. Tube fossils from gossanites of the Urals VHMS deposits, Russia: Authigenic mineral assemblages and trace element distributions. *Ore Geol. Rev.* **2017**, *85*, 107–130. [[CrossRef](#)]
31. Vikentyev, I.V.; Belogub, E.V.; Novoselov, R.A.; Moloshag, V.P. Metamorphism of volcanogenic massive sulphide deposits in the Urals. *Ore Geol. Rev.* **2017**, *85*, 30–63. [[CrossRef](#)]
32. Kontar, E.S. Quantitative estimation of massive sulfide ore formation. *Geol. Ore Dep.* **2002**, *44*, 543–555.
33. Zaykov, V.V. *Volcanism and Sulfide Mounds of Paleocene Margins (After the Example of Ural's and Siberia's Massive Sulfide-Bearing Zones)*; Nauka: Moscow, Russia, 2006; 428p. (In Russian)
34. Koroteev, V.A.; Yazeva, R.G.; Bochkarev, V.V. *Geological Structure and Composition of Sulfide Ores of the Safyanov'ka Deposit (Middle Urals)*; IGG UB RAS: Ekaterinburg, Russia, 1997; 49p. (In Russian)
35. Yazeva, R.G.; Moloshag, V.P.; Bochkarev, V.V. Geology and ore mineral assemblages of the Saf'yanovka massive sulfide deposit in the Central Urals retrooverthrust. *Geol. Rudn. Mestorozhd.* **1991**, *33*, 58–76. (In Russian)
36. Maslennikova, S.P.; Maslennikov, V.V. *Paleozoic Black Smoker Sulfide Chimneys*; UB RAS: Yekaterinburg, Russia, 2007; 312p. (In Russian)
37. Maslennikov, V.V. *Sedimentogenesis, Halmyrolysis and Ecology of Massive Sulfide Paleohydrothermal Fields*; Geotur: Miass, Russia, 1999; 348p. (In Russian)
38. Prokin, V.A.; Buslaev, F.P.; Ismagilov, M.I. *Copper Massive Sulfide Deposits of the Urals: Geological Structure*; Ural Branch of the RAS: Sverdlovsk, Russia, 1988; 241p. (In Russian)
39. Maslennikov, V.V.; Ayupova, N.R.; Herrington, R.J.; Danyushevskiy, L.V.; Large, R.R. Ferruginous and manganiferous haloes around massive sulphide deposits of the Urals. *Ore Geol. Rev.* **2012**, *47*, 5–41. [[CrossRef](#)]
40. Zaykov, V.V.; Melekestseva, I.Y.; Artemyev, D.A.; Yuminov, A.M.; Simonov, V.A.; Dunaev, A.Y. *Geology and Massive Sulfide Mineralization of the Southern Flank of the Main Uralian Fault*; Geotur: Miass, Russia, 2009; 376p. (In Russian)
41. Longerich, H.P.; Jackson, S.E.; Gunter, D. Inter-laboratory note: Laser ablation inductively coupled plasma mass spectrometric transient signal data acquisition and analyte concentration calculation. *J. Anal. Atomic Spectrom.* **1996**, *11*, 899–904. [[CrossRef](#)]
42. Danyushevsky, L.; Robinson, P.; Gilbert, S.; Norman, M.; Large, R.R.; McGoldric, P.; Shelley, M. Routine quantitative multi-element analysis of sulphide minerals by laser ablation ICP-MS: Standard development and consideration of matrix effect. *Geochim. Explor. Environ. Anal.* **2011**, *11*, 51–60. [[CrossRef](#)]
43. Wilson, S.A.; Ridley, W.I.; Koenig, A.E. Development of sulphide calibration standards for the laser ablation inductively-coupled plasma mass spectrometry technique. *J. Anal. Spectrom.* **2002**, *17*, 406–409. [[CrossRef](#)]
44. Ayupova, N.R.; Maslennikov, V.V.; Artem'ev, D.A.; Blinov, I.A. Mineralogical and geochemical features of pyrite nodules from sulfide turbidites in the Talgan Cu–Zn massive sulfide deposit (Southern Urals). *Lithol. Miner. Res.* **2019**, *54*, 447–464. [[CrossRef](#)]
45. Smirnov, V.I. *Correlation Methods in Paragenetic Analysis*; Nedra: Moscow, Russia, 1981; 174p. (In Russian)
46. Yaroslavtseva, N.S.; Maslennikov, V.V.; Safina, N.P.; Leshchev, N.V.; Soroka, E.I. Carbon-bearing siltstones of the Saf'yanovskoe Cu–Zn massive sulfide deposit (Central Urals). *Litosfera* **2012**, *2*, 106–125. (In Russian)

47. Ayupova, N.R.; Maslennikov, V.V.; Filippova, K.A. REE geochemistry and mineralogy in ores of the Talgan Cu–Zn massive sulfide deposit, Southern Urals. *Dokl. Earth Sci.* **2019**, *487*, 973–975. [[CrossRef](#)]
48. Fairbridge, R.W. Syndiagenesis-anadiagenesis-epidiagenesis: Phase of lithogenesis. In *Diagenesis in Sediments and Sedimentary Rocks*; Larsen, G., Chilingar, G.V., Eds.; Elsevier: Amsterdam, The Netherlands; London, UK; New York, NY, USA, 1983; Volume 2, pp. 17–114.
49. Goodfellow, W.D.; Peter, J.M.; Winchester, J.A.; Van Staal, C.R. Ambient marine environment and sediment provenance during formation of massive sulfide deposits in the Bathurst Mining Camp: Importance of reduced bottom waters to sulfide precipitation and preservation. *Econ. Geol. Monogr.* **2003**, *11*, 129–156. [[CrossRef](#)]
50. Wilkin, R.T.; Barnes, H.L. Formation processes of framboidal pyrite. *Geochim. Cosmochim. Acta* **1997**, *61*, 323–339. [[CrossRef](#)]
51. Lin, Q.; Wang, J.; Algeo, T.J.; Sun, F.; Lin, R. Enhanced framboidal pyrite formation related to anaerobic oxidation of methane in the sulfate-methane transition zone of the northern south China sea. *Mar. Geol.* **2016**, *379*, 100–108. [[CrossRef](#)]
52. Fairbridge, R.W. Phases of diagenesis and authigenesis. In *Diagenesis in Sediments*; Larsen, G., Chilingar, G.V., Eds.; Elsevier: Amsterdam, The Netherlands, 1967; pp. 19–89.
53. Velde, B.; Medhioub, M. Approach to chemical equilibrium in diagenetic chlorites. *Contrib. Mineral. Petrol.* **1988**, *98*, 122–127. [[CrossRef](#)]
54. Harvey, C.C.; Browne, P.R.L. Mixed-layer clay geothermometry in the Wairakei geothermal field, New Zealand. *Clays Clay Miner.* **1991**, *39*, 614–621. [[CrossRef](#)]
55. Jahred, J.S.; Aagaard, P. Compositional variations in diagenetic chlorites and illites and relationships with formation-water chemistry. *Clay Miner.* **1989**, *24*, 157–170. [[CrossRef](#)]
56. Lindgreen, H.; Drits, V.A.; Sakharov, B.A.; Jakobsen, H.J.; Salyn, A.L.; Dainyak, L.G.; Kroyer, H. The structure and diagenetic transformation of illite-smectite and chlorite-smectite from North Sea Cretaceous-Tertiary chalk. *Clay Miner.* **2002**, *37*, 429–450. [[CrossRef](#)]
57. Lanson, B.; Sakharov, B.; Claret, F.; Drits, V. Diagenetic smectite-to-illite transition in clay-rich sediments: A reappraisal of X-Ray diffraction results using the multi-specimen method. *Am. J. Sci.* **2009**, *309*, 476–516. [[CrossRef](#)]
58. Gregory, D.; Cracknell, M.; Large, R.; McGoldrick, P.; Kuhn, S.; Maslennikov, V.; Baker, M.; Fox, N.; Belousov, I.; Figueroa, M.; et al. Distinguishing ore deposit type and barren sedimentary pyrite using laser ablation-inductively coupled plasma-mass spectrometry trace element data and statistical analysis of large data sets. *Econ. Geol.* **2019**, *114*, 771–786. [[CrossRef](#)]
59. Kuznetsov, V.; Maksimov, F.; Zhelezov, A.; Cherkashov, G.; Bel'tenev, V.; Lazareva, L. <sup>230</sup>Th/U chronology of ore formation within the Semyenov hydrothermal district (13°31' N) at the Mid-Atlantic Ridge. *Geochronometria* **2011**, *38*, 72–76. [[CrossRef](#)]
60. Brumsack, H.-J. Geochemistry of recent TOC-rich sediments from the Gulf of California and the Black Sea. *Geol. Rundsch.* **1989**, *78*, 851–882. [[CrossRef](#)]
61. Zierenberg, R.A.; Kost, R.A.; Morton, J.L.; Bouse, R.M. Genesis of massive sulfide deposit on a sediment-covered spreading center, Escanaba trough, Southern Gorda Ridge. *Econ. Geol.* **1993**, *88*, 67–81. [[CrossRef](#)]
62. Gaspar, O.C. Mineralogy and sulfide mineral chemistry of the Neves-Corvo ores, Portugal: Insight into their genesis. *Can. Mineral.* **2002**, *40*, 611–632. [[CrossRef](#)]
63. Ayupova, N.R.; Melekestseva, I.Y.; Maslennikov, V.V.; Tseluyko, A.S.; Blinov, I.A.; Beltenev, V.E. Uranium accumulation in modern and ancient Fe-oxide sediments: Examples from the Ashadze-2 hydrothermal sulfide field (Mid-Atlantic Ridge) and Yubileynoe massive sulfide deposit (South Urals, Russia). *Sediment. Geol.* **2018**, *367*, 164–174. [[CrossRef](#)]
64. Butler, I.B.; Nesbitt, R.V. Trace element distribution in the chalcopyrite wall of a black smoker chimney: Insights from laser ablation inductively coupled plasma mass spectrometry (LA-ICP-MS). *Earth Planet. Sci. Lett.* **1999**, *167*, 335–345. [[CrossRef](#)]
65. Maslennikov, V.V.; Maslennikova, S.P.; Large, R.R.; Danyushevsky, L.V. Study of trace element zonation in vent chimneys from the Silurian Yaman-Kasy VMS (the Southern Urals, Russia) using laser ablation inductively coupled plasma mass spectrometry (LA-ICP MS). *Econ. Geol.* **2009**, *104*, 1111–1141. [[CrossRef](#)]
66. Safina, N.P.; Maslennikov, V.V. Lithological-mineralogical zonality of sulfide cycloites of the Yaman-Kasy and Safyanovskoye massive sulfide deposits. *Dokl. Earth. Sci.* **2008**, *419*, 423–434. [[CrossRef](#)]

67. Melekestseva, I.Y.; Tret'yakov, G.A.; Nimis, P.; Yuminov, A.M.; Maslennikov, V.V.; Maslennikova, S.P.; Kotlyarov, V.A.; Beltenev, V.E.; Danyushevsky, L.V.; Large, R. Barite-rich massive sulfides from the Semenov-1 hydrothermal field (Mid-Atlantic Ridge, 13°30.87' N): Evidence for phase separation and magmatic input. *Mar. Geol.* **2014**, *349*, 37–54. [[CrossRef](#)]
68. Huston, D.L.; Sie, S.H.; Suter, G.F.; Cooke, D.R.; Both, R.A. Trace elements in sulfide minerals from Eastern Australian volcanic-hosted massive sulfide deposits. Part I, Proton microprobe analyses of pyrite, chalcopyrite, and sphalerite, and Part II. Selenium levels in pyrite comparison with  $\delta S_{34}$  values and implication for the source of sulfur in volcanogenic hydrothermal systems. *Econ. Geol.* **1995**, *90*, 1167–1196. [[CrossRef](#)]
69. Clark, L.A. The Fe–As–S system—Phase relations and applications. *Econ. Geol.* **1960**, *55*, 1345–1381. [[CrossRef](#)]
70. Kumar, R.; Ray, R.K.; Biswas, A.K. Physico-chemical nature and leaching behaviour of goethites containing Ni, Co and Cu in the sorption and coprecipitation mode. *Hydrometallurgy* **1990**, *25*, 61–83. [[CrossRef](#)]
71. Kreissl, S.; Bolanz, R.; Gottlicher, J.; Steininger, R.; Tarassov, M.; Markl, G. Structural incorporation of W6+ into hematite and goethite: A combined study of natural and synthetic iron oxides developed from precursor ferrihydrite and the preservation of ancient fluid compositions in hematite. *Am. Mineral.* **2016**, *101*, 2701–2715. [[CrossRef](#)]
72. Dai, C.; Lin, M.; Hu, Y. Heterogeneous Ni- and Cd-bearing ferrihydrite precipitation and recrystallization on quartz under acidic pH condition. *ACS Earth Space Chem.* **2017**, *110*, 621–628. [[CrossRef](#)]



© 2020 by the authors. Licensee MDPI, Basel, Switzerland. This article is an open access article distributed under the terms and conditions of the Creative Commons Attribution (CC BY) license (<http://creativecommons.org/licenses/by/4.0/>).